Actinomycin D and bortezomib disrupt protein homeostasis in Wilms tumor

Patricia D.B. Tiburcio[1], Kenian Chen[2], Lin Xu[1,2], Kenneth S. Chen[1,3 *]

[1] Department of Pediatrics, University of Texas Southwestern Medical Center, Dallas, TX
[2] Quantitative Biomedical Research Center, Peter O'Donnell School of Public Health, University of Texas Southwestern Medical Center, Dallas, TX
[3] Children's Medical Center Research Institute, University of Texas Southwestern Medical Center, Dallas, TX

* Correspondence: Kenneth S. Chen, UT Southwestern Medical Center, 5323 Harry Hines Blvd., Dallas, TX 75390; phone: +1-214-648-8291; email: Kenneth.Chen@UTSouthwestern.edu

The authors have no conflicts of interest to disclose.

ABSTRACT

Wilms tumor is the most common kidney cancer in children, and diffuse anaplastic Wilms tumor is the most chemoresistant histological subtype. Here, we explore how Wilms tumor cells evade the common chemotherapeutic drug actinomycin D, which inhibits ribosomal RNA biogenesis. Using ribosome profiling, protein arrays, and a genome-wide knockout screen, we describe how actinomycin D disrupts protein homeostasis and blocks cell cycle progression. We found that, when ribosomal capacity is limited by actinomycin D treatment, anaplastic Wilms tumor cells preferentially translate proteasome components and upregulate proteasome activity. Based on these findings, we tested whether the proteasome inhibitor bortezomib sensitizes cells to actinomycin D treatment. Indeed, we found that the combination induces apoptosis both *in vitro* and *in vivo* and prolongs survival in xenograft models. Lastly, we show that increased levels of proteasome components are associated with anaplastic histology and worse prognosis in Wilms tumor patients. In sum, maintaining protein homeostasis is critical for Wilms tumor proliferation, and it can be therapeutically disrupted by blocking protein synthesis or turnover.

36 **INTRODUCTION**

37

38 Wilms tumors, or nephroblastomas, are the most common pediatric kidney cancer.
39 Globally, Wilms tumor is diagnosed in 10.4 per 1 million children less than 15 years old each
40 year [1]. North American risk stratification criteria classify Wilms tumors as having favorable or
41 anaplastic histology. The development of effective combinations of chemotherapy, radiation,
42 and surgery has pushed the 5-year overall survival rate to over 90% for those with favorable
43 histology Wilms tumor (FHWT). These strong cure rates have allowed us to de-intensify therapy
44 for some patients with FHWT, where up to 24% of long-term survivors who were treated on
45 historical regimens developed therapy-related chronic health conditions [2]. Other FHWT patients
46 receive intensified therapy based on biological risk factors such as combined loss-of-
47 heterozygosity (LOH) of chromosomes 1p and 16q or gain of chromosome 1q. On the other
48 hand, patients with diffuse anaplastic Wilms tumor (DAWT), which accounts for ~10% of Wilms
49 tumor patients, continue to have a relapse rate of over 40% and a 4-year overall survival rate of
50 66% despite being treated with more aggressive drugs such as doxorubicin, etoposide,
51 cyclophosphamide, and carboplatin [1,3-5]. Recent attempts to intensify chemotherapy for those
52 with DAWT have increased short-term toxicity with minimal improvements in cure rate [6].
53 Anaplastic histology is associated with loss or mutation of p53 [7,8], but the molecular
54 mechanisms underpinning chemoresistance in anaplasia are unknown, and there remain no
55 targeted therapies effective in Wilms tumor.
56 Since the 1960s, chemotherapy regimens utilizing actinomycin D (actD), also called
57 dactinomycin, have been routinely used to treat Wilms tumors [9,10], rhabdomyosarcoma, and
58 other sarcomas [11,12]. In DAWT, however, actD has been removed from standard protocols. Unlike
59 most FHWT regimens, DAWT patients receive doxorubicin, which can provide higher rates of
60 cure but carries more short- and long-term toxicities, including cardiotoxicity and secondary
61 cancers [13]. Understanding how to improve actD sensitivity without the toxicities associated with
62 anthracyclines like doxorubicin could improve outcomes for Wilms tumor as well as other
63 malignancies.

64 The molecular activity of actD is concentration-dependent. At high concentrations, it is a
65 DNA-intercalating agent that can block transcription and DNA replication. However, at the low-
66 nanomolar serum concentrations typically achieved in patients, it primarily inhibits transcription
67 of ribosomal RNA (rRNA), which is transcribed by RNA polymerase I (Pol I), and transfer RNA
68 (tRNA), which is transcribed by RNA polymerase III (Pol III) [14-18]. Ribosomes are composed of
69 rRNA and ribosomal proteins (RP), and impaired Pol I activity results in fewer fully formed
70 ribosomes, which consequently reduces global translation. In ribosome-depleted settings, the
71 remaining ribosomes are not uniformly distributed across remaining transcripts; instead, they
72 favor certain transcripts, based on factors such as their intracellular localization, secondary
73 structure, and presence of specific sequence motifs [18,19] (Figure 1A). We thus reasoned that the
74 genes preferentially translated following actD exposure could be therapeutically targetable in
75 anaplastic Wilms tumor . To date, however, no published findings have characterized how actD
76 affects translation in Wilms tumors.
77 In this study, we used ribosome profiling to find that proteasome components are
78 preferentially translated in anaplastic Wilms tumor cell lines following actD treatment. Based on
79 these findings, we studied a combination with the proteasome inhibitor bortezomib (BTZ), and
80 we found that it increases sensitivity of anaplastic Wilms tumor cells to actD *in vitro* and *in vivo*.
81 Lastly, DAWTs express higher transcript levels of several proteasome components than relapsed
82 FHWTs, and higher levels of proteasome components are associated with worse prognosis.
83

84 **RESULTS**

85

86 **Actinomycin D alters the translational landscape of anaplastic Wilms tumor cells**

87

88 ActD blocks rRNA transcription at nanomolar doses and mRNA transcription at
89 micromolar doses [18]. To examine the effect of actD on cell viability at nanomolar doses in Wilms
90 tumor, we measured 72-hour actD sensitivity in two anaplastic Wilms tumor cell lines, WiT49
91 and 17.94 (Supplementary Figure S1A). For these cell lines, we measured IC50 to be 1.3 and 2.2
92 nM, respectively. Next, we confirmed that 2 nM actD reduces levels of 45s pre-rRNA and 18s
93 mature rRNA in both cell lines (Supplementary Figure S1B). This results in decreased overall
94 protein synthesis, consistent with specific impairment of Pol I activity, as measured by
95 incorporation of both the methoinine analog L-azidohomoalanine and O-propargyl-puromycin
96 (Figure 1B, Supplementary Figure S1C, S1D).
97 Thus, to understand how actD affects protein levels and cellular functions in Wilms
98 tumor, we next performed three complementary assays in parallel: ribosome profiling, to
99 identify preferentially translated transcripts; reverse-phase protein arrays (RPPA), to identify
100 differences in protein levels and post-translational modifications; and a CRISPR dropout screen,
101 to identify targetable vulnerabilities.
102 First, to ascertain preferentially translated transcripts, we used ribosome profiling (also
103 known as ribosome footprinting), which provides a snapshot of the transcripts actively
104 undergoing translation [20,21]. This technique entails trapping ribosomes on mRNA transcripts,
105 degrading unprotected RNA, and sequencing the RNA fragments that were protected from
106 degradation by ribosomes. Sequencing of the ribosome-protected RNA is computationally
107 compared to RNA sequenced conventionally in the same samples to calculate "translational
108 efficiency", a measure of the active translation of each transcript.
109 Specifically, we performed ribosome profiling in WiT49 cells treated with actD or vehicle
110 control at 6 hours, 72 hours, and two weeks. At each timepoint, we performed ribosome
111 profiling to quantify gene-level differences in translational efficiency in actD- versus vehicle-
112 treated cells. To confirm the expected effect of depleting ribosomes, we examined the locations

113 of the ribosome footprint edges in metagene plots around translation start sites
114 (Supplementary Figure S2A-S2F). As expected, in both DMSO- and actD-treated cells, there were
115 essentially no detectable reads in 5' untranslated regions (5'UTRs), while coding sequences
116 exhibit a trinucleotide periodicity, reflecting the reading frame of elongating ribosomes. In
117 DMSO-treated cells, the left edge of ribosome footprints accumulated just upstream of
118 translation start sites, which reflects pausing of the ribosome at the initiation site, as expected
119 for normal conditions (Supplementary Figure S2A-S2C). In actD-treated cells, however, the
120 initiation site peak was blunted, suggesting that when ribosomes are depleted, the ribosomes
121 that remain spend less time paused at initiation (Supplementary Figure S2D-S2F). For all
122 durations of treatment, actD appeared to have minimal effect on the transcriptome, while
123 ribosome footprints revealed gross perturbation of translational landscapes by actD
124 (Supplementary Figure S3A-S3B). After two weeks of intermittent actD dosing, cells appear to
125 return to a new steady state with globally reduced translation.
126 We next compared the translational efficiency of each gene in actD-treated cells at 6 and
127 72 hours, and we connected preferentially translated genes into Kyoto Encyclopedia of Genes
128 and Genomes (KEGG) pathways using GSEA (Supplementary Table S1). The most enriched KEGG
129 pathway by translational efficiency at both timepoints was KEGG_RIBOSOME, which is
130 composed of RPs and genes that regulate ribosome biosynthesis (Figures 1B, 1C; Supplementary
131 Figures S4A, S4B; Supplementary Table S2). This is consistent with reports that RPs are unstable
132 when actD depletes rRNA, which can upregulate translation of RPs via mTORC1 signaling [22,23].
133 This increase in translational efficiency was accompanied by a relative decrease in mRNA
134 abundance for ribosomal proteins (Supplementary Figure S4C). KEGG_PROTEASOME was the
135 only other gene set in the top five most preferentially translated gene sets at both timepoints
136 (Figure 1C, 1D; Supplementary Figure S4D, S4E; Supplementary Table S2). This increase in
137 translational efficiency was also accompanied by a relative decrease in mRNA abundance for
138 proteasomal proteins (Supplementary Figure S4F). On the other hand, the most downregulated
139 gene sets at 6 hours entailed nucleotide turnover, which led to a depletion of cell cycle genes at
140 72 hours (Figure 1C, 1D; Supplementary Table S2). In sum, our ribosome profiling of actD-

141 treated cells detected preferential translation of RPs and proteasome components, with a
142 concomitant decrease in translation of cell cycle genes.
143 Next, we used a genome-wide CRISPR screen to identify therapeutic vulnerabilities in
144 cells with intermittent actD or DMSO for 14 days. We again used KEGG pathways to categorize
145 dependency genes (Figure 1E; Supplementary Table S3). Here, we again found enrichment for
146 pathways related to protein turnover, including KEGG_PROTEASOME, as well as nucleic acid
147 turnover and cell cycle.
148 Thirdly, since actD regulates protein synthesis, we also performed RPPA on WiT49 cells
149 treated with actD or DMSO for 72 hours to understand how actD affects protein levels and post-
150 translational modifications (Figure 1F; Supplementary Table S4). We found an increase in
151 phosphorylation of some components of the mTORC1 signaling pathway, which mediates the
152 feedback signaling to upregulate translation of RPs in the setting of rRNA depletion [23]. On the
153 other hand, cell cycle markers such as CDT1, CDC6, and phosphorylated RB1 were depleted in
154 actD-treated cells (also see Figure 3D below). This is consistent with depletion of cell cycle gene
155 sets in ribosome profiling at 72 hours. Together, our three datasets show that, in the presence
156 of actD, Wilms tumor cells choose to preferentially translate ribosome and proteasome
157 components rather than progress through the cell cycle.
158
159 **mTORC1 inhibition does not sensitize Wilms tumor cells to actinomycin D**
160 Based on phosphorylation of mTORC1 signaling intermediates in RPPA results and prior
161 interest in mTORC1 signaling in Wilms tumor [24,25], we next investigated how actD affected
162 mTORC1 signaling in WiT49 and a second anaplastic Wilms tumor cell line, 17.94. Using Western
163 blots, we confirmed that actD induced phosphorylation of AKT and 4E-BP1 in WiT49 and 17.94
164 cells (Supplementary Figure S4G, S4H). (The phosphorylation of another mTORC1 target,
165 p70S6K, was not clearly upregulated by actD.) We treated WiT49 and 17.94 with rapamycin at
166 doses up to 100 µM and found that this drug confers a more cytostatic rather than cytotoxic
167 effect (Supplemental Figure S4I). We also measured cell viability in combinations of actD and
168 the mTORC1 inhibitor rapamycin using the Loewe independence model (Supplementary Figure
169 S4J). However, the interaction did not consistently show synergy, as we only observed synergy

170 above the upper limit of serum concentrations typically achieved in patients (~2-3 nM for actD[14]
171 and 16 nM for rapamycin[26]). In other words, mTORC1 inhibition with rapamycin did not appear
172 to consistently sensitize Wilms tumor cells to actD, and rapamycin alone was not cytotoxic, even
173 at very high doses.
174
175 **ActD induces proteotoxic stress and cell cycle arrest in anaplastic Wilms tumor cells**
176 One effect of mTORC1 signaling is to upregulate translation of RPs [27], and
177 KEGG_RIBOSOME was the most enriched gene set in actD-treated cells. However, we found that
178 72-hour actD treatment in fact appeared to slightly reduce the total protein levels of multiple
179 RPs in both WiT49 and 17.94 (Supplementary Figure S5A, S5B). This could be because excess RP
180 subunits are unstable without rRNA and are degraded by the proteasome to maintain
181 appropriate RP:rRNA stoichiometry [22,28,29].
182 While we did not observe an increase in RP levels with actD treatment, we did observe
183 accumulation of proteasome components. When we exposed WiT49 and 17.94 to actD for up to
184 72 hours, both cell lines exhibited an appreciable increase in several proteasome complex
185 subunits at one or more timepoints between 18 and 72 hours (Figure 2A, 2B). We specifically
186 measured PSMD1 (also known as P112), PSMA6 (subunit α1), PSMB1 (β6), PSMB2 (β4), and
187 PSMB5 (β5), as well as the molecular chaperone for proteasome assembly, POMP. In both cell
188 lines, PSMA6, PSMD1, and POMP peaked at 18-24 hours. PSMB1 peaked at 72h in WiT49 and
189 but rose earlier in 17.94 and remained high, while PSMB2 peaked at 24h in 17.94 but rose
190 earlier in WiT49 and remained high. Lastly, PSMB5 peaked at 48-72 hours in WiT49 but did not
191 appear to rise in 17.94 at the timepoints we examined. These increases in protein levels of
192 proteasome components corresponded to increased proteasome chymotrypsin-like enzymatic
193 activity in both cell lines, which was blunted by co-treatment with the proteasome inhibitor
194 bortezomib (BTZ, Figure 2C).
195 Because actD caused preferential translation of proteasome subunits, we next examined
196 how WiT49 and 17.94 respond to proteasome inhibition. These two cell lines were sensitive to
197 BTZ alone at nanomolar concentrations, in the range of serum levels typically achieved in
198 patients [30,31] (Figure 3A). This is close to the average sensitivity (3.9 nM) observed across the

199 NCI-60 cell lines screen [32]. Furthermore, at or below these levels, actD and BTZ synergistically
200 inhibited WiT49 and 17.94 to different degrees (Figure 3B). In WiT49, actD and BTZ acted
201 synergistically across nearly all combination concentrations. Loewe scores in 17.94 showed
202 synergy at lower concentrations and additivity at medium and higher concentrations. Taken
203 together, these data suggest that the addition of BTZ could be a strategy to enhance or restore
204 actD sensitivity in anaplastic Wilms tumor cells.

205 Our RPPA results (Fig. 1F) had shown a reduction in cell cycle markers in actD-treated
206 WiT49, so we next examined how actD and BTZ affect cell cycle progression using flow
207 cytometry (Figure 3C). Specifically, we treated WiT49 and 17.94 with actD and/or BTZ for 48
208 hours, and we measured the proportion of cells in each phase of the cell cycle using flow
209 cytometry (Figure 3C). We found that actD increased the proportion of cells in G0/G1 and
210 reduced the proportion in the S phase in both cell lines, though the difference was only
211 statistically significant in WiT49. This is consistent with previous reports that low-dose actD
212 treatment leads to G1 pause [33,34]. In contrast, BTZ increased the proportion of cells in G2 and
213 reduced the proportion in the S phase, consistent with previous reports that BTZ causes cells to
214 accumulate in G2/M phase [32].

215 BTZ has previously been shown to trigger cell death, cell cycle arrest, and autophagy in
216 cancer cell lines [35-40], so we next measured cell cycle and apoptosis markers using Western
217 blots. In both cell lines, actD alone reduces cell cycle markers, including chromatin licensing and
218 DNA replication factor 1 (CDT1), cyclin D2, cyclin E1, and cyclin A2 (Figure 3D) [41-43]. These cell
219 cycle regulators are synthesized and degraded in each turn of the cell cycle [44,45]. These support
220 our findings from CRISPR screen and protein arrays, which showed that actD induced a
221 dependency on cell cycle genes and led to a fall in cell cycle markers (Figures 1E, 1F). In addition
222 to impaired cell cycle progression, use of the proteasome inhibitor BTZ resulted in the
223 accumulation of apoptotic markers in both cell lines (Figure 3D) [46-49]. ActD alone induced a
224 slight increase in cleaved caspase-7 and cleaved PARP in 17.94 cells, but both apoptosis markers
225 were dramatically induced by BTZ in both cell lines. The combination of these effects supports
226 the potential for using actD and BTZ to target anaplastic Wilms tumors.
227

228 **Combined treatment of actinomycin D and bortezomib in Wilms tumor xenografts suppresses**
229 **growth *in vivo***
230 We next examined the effect of combining BTZ with actD against two anaplastic Wilms
231 tumor lines *in vivo*: cell line-derived xenografts from 17.94 and the *TP53*-mutated patient-
232 derived xenograft (PDX) line KT-53 [50,51]. We implanted both lines into NSG mice and treated
233 them with vehicle only, actD, BTZ, or both. We found that combination treatment significantly
234 reduced tumor volume and conferred a significant survival advantage for mice bearing KT-53
235 xenografts compared to the other three arms (Figure 4A, 4B). Similarly, 17.94 xenografts treated
236 with the combination of actD and BTZ were significantly smaller than those who received
237 vehicle control or BTZ alone (Figure 4C, 4D). (Although it did not reach statistical significance,
238 tumor volume in the combination treatment cohort was also slightly smaller than the actD-only
239 arm.) In these treatments, BTZ was well tolerated and did not appear to add toxicity. There was
240 no difference in body weight between mice receiving BTZ and vehicle (Supplementary Figure
241 S6A, S6B). Similarly, the weights of mice treated with the combination of actD and BTZ was
242 similar to the weights of mice treated with actD alone.
243 Based on the effects of actD and BTZ on cell cycle and apoptosis we had observed *in*
244 *vitro*, we next measured cell cycle and apoptosis markers in these subcutaneous tumors. We
245 used immunohistochemistry for Ki-67 as a marker of proliferation and terminal
246 deoxynucleotidyl transferase dUTP nick-end labeling (TUNEL) assay as a marker of apoptosis. In
247 both lines, tumors from combination-treated mice had a statistically significant reduction in
248 proliferation compared to vehicle or BTZ alone (Figure 4E, Supplemental Figure S7A-S7D).
249 Similarly, in both lines, combination treatment yielded significantly more apoptosis than vehicle
250 and actD alone (Figure 4F, Supplemental Figure S7E, S7F). Taking these into consideration, we
251 find that the compounding effects of adding BTZ to actD could be a powerful approach to
252 targeting anaplastic Wilms tumor cells.
253
254 **Proteasome subunit expression levels correlate with outcome**
255 Lastly, we examined expression of proteasome genes in publicly available RNA-seq data
256 from 42 DAWT and 83 relapsed FHWT (rFHWT) samples generated by the NCI Therapeutically

257 Applicable Research to Generate Effective Treatments (TARGET) project [8]. Compared to rFHWT,
258 the single most enriched KEGG gene set in DAWT was KEGG_PROTEASOME (Figure 5A,
259 Supplementary Figure S8A, Supplementary Table S6). Similarly, two of the three most enriched
260 Reactome gene sets were related to APC/C-mediated degradation of cell cycle proteins,
261 suggesting that proteasomal degradation could promote proliferation in DAWT by degrading
262 proteins in each cell cycle (Figure 5B, Supplementary Figure S8B, Supplementary Table S6).
263 Next, we examined whether expression of proteasome subunits correlated with
264 outcome in Wilms tumor. We stratified rFHWT and DAWT patients into three categories based
265 on high, medium, or low expression of the enzymatic proteasome subunits *PSMB5* (β5), *PSMB6*
266 (β1), and *PSMB7* (β2) based on expression z-scores for each gene. Tumors with at least one
267 gene z-score ≥ +1 were categorized as "high", while those with at least one gene z-score ≤ -1
268 were categorized as "low". Samples with z-scores between -1 and +1 for all three genes were
269 categorized as "medium", while those with one gene z-score ≥ +1 and another gene z-score ≤ -1
270 were omitted.
271 Among rFHWT patients, proteasome-high patients fared far worse than proteasome-low
272 or proteasome-medium patients (Figure 5C, Supplementary Figure S9A). However, this is a
273 clinically heterogeneous population comprised of patients who would have received different
274 treatments based on clinical stage, chromosomal loss-of-heterozygosity, and other factors. Thus,
275 we next examined whether proteasome expression correlated with survival within each clinical
276 stage. To increase statistical power, we combined the proteasome-low and proteasome-medium
277 groups, which fared similarly to each other (Figure 5C). We then compared the survival of the
278 proteasome-high group to the combined proteasome-low and proteasome-medium group
279 within each stage (Supplementary Figures S9B-S9E). We found that high proteasome gene
280 expression still correlated with significantly worse outcome in Stages II and IV (p=0.007 and
281 0.002, respectively). Although the correlation was not significant for the other groups, these
282 analyses were limited by small sample sizes after subdividing by stage and proteasome
283 expression. There was only one proteasome-high patient in the Stage I rFHWT cohort. In the
284 Stage III rFHWT cohort, proteasome-high patients fared slightly worse but did not reach
285 statistical significance (p=0.15).

286 Among DAWT patients, who do not usually receive actD-based therapy regimens, the
287 relationship between proteasome expression and outcome was less evident; proteasome-
288 medium patients fared worse than proteasome-low patients, but proteasome-high patients
289 were not significantly different from proteasome-medium or -low [8,52,53] (Figure 5D). Together,
290 these data suggest that proteasome subunit levels may underlie some of the clinical differences
291 between DAWT and FHWT, and that high proteasome subunit levels correlate with poorer
292 prognosis in rFHWT. Proteasome levels could be prognostic in some subgroups, and proteasome
293 inhibition could benefit some of these patients.

294 **DISCUSSION**

295

296 Developments in Wilms tumor research have illuminated the mutational, epigenetic,
297 mRNA, and miRNA expression landscapes of these tumors, yet relevant targetable
298 vulnerabilities remain elusive [8,54-58]. Anaplastic Wilms tumors exhibit relative resistance to
299 conventional chemotherapy, including actD, and little is known about how to overcome such
300 resistance. Furthermore, despite its widespread use, little is known about how actD influences
301 the translational landscape of cancer. Defining the mechanisms underlying these effects and
302 their consequences could potentially uncover targetable vulnerabilities in relatively chemo-
303 refractory anaplastic Wilms tumors, which could enhance outcomes while minimizing off-target
304 toxicities in survivors. Through several orthogonal approaches, our work reveals that actD
305 disrupts protein homeostasis in Wilms tumor and suggests proteasome inhibition as a potential
306 targeted therapy for inducing actD sensitivity in anaplastic Wilms tumors.

307 Protein homeostasis involves a synchronized and responsive balance between protein
308 synthesis and degradation, which are both affected by actD. Since protein synthesis is energy-
309 intensive, particularly in rapidly proliferating cancers where proteins like cyclins are
310 continuously synthesized and degraded, maintaining protein homeostasis is crucial to ensure
311 optimal levels of amino acids and other nutrients for growth [59-61]. Blocking protein synthesis
312 with actD leads cells to upregulate Akt/mTORC1 signaling, which can increase the translation of
313 ribosomal protein (RP) genes [27,62-64]. Although we detected an increase in translational
314 efficiency of RP genes, they did not accumulate by Western blot in our 72-hour treatments,
315 possibly due to their instability without rRNA. Although the mTOR pathway is a potential
316 therapeutic target in Wilms tumor and other cancers [65-67], the combination of actD and
317 rapamycin did not consistently show synergy *in vitro* for either cell line, and rapamycin alone
318 only exhibited a cytostatic effect. Our cells were in nutrient-rich media which may be
319 compounding to the variables that dictate the effect of rapamycin [66,68], and our results do not
320 rule out the possibility that other mTOR signaling inhibitors could still have potential.

321 The importance of protein homeostasis in Wilms tumor is also supported by other
322 recent findings. Common Wilms tumor mutations interfere with protein homeostasis. For
323 instance, recurrent mutations in *CTNNB1* and *MYCN* prolong their stability by interfering with

324 their degradation by the proteasome [8,69]. Other common mutations impair processing of
325 microRNAs, which normally regulate translation of target transcripts [54,57,58,70]. Recently, a small-
326 molecule inhibitor of histone lysine demethylases KDM4A-C was found to act by reducing rRNA
327 and RP transcripts in WiT49 cells, which led to a broad reduction in protein translation[71]. How
328 actD or BTZ interacts with common Wilms tumor mutations or with KDM4A-C inhibition remains
329 to be seen.

330 Based on our finding that proteasome subunits were preferentially translated after actD
331 exposure, we found that proteasome inhibition with BTZ sensitizes cells to actD *in vitro* and *in*
332 *vivo*. The proteasome is upregulated in response to proteotoxic stresses [28,29,72], and
333 Akt/mTORC1 activates proteasome subunit expression via *Nrf1/NFE2L1* [73-76] to enhance the
334 intracellular amino acid pool and the unfolded protein response. BTZ was the first proteasome
335 inhibitor approved by the United States Food and Drug Administration [77-79], and it has been
336 tested in pediatric cancer patients [30,80,81]. However, other than a study showing a lack of cross-
337 resistance between actD and BTZ in gliobastoma [82], no published studies have explored
338 combinatorial treatment of actD and BTZ to our knowledge.

339 While proteasome inhibitors have been clinically successful in hematological cancers,
340 single-agent proteasome inhibitor trials have not been as successful for solid tumors [83,84]. It is
341 thought that this could be due to insufficient pharmacokinetic distribution of BTZ. Strategies for
342 enhancing the effect of BTZ in solid tumors include liposomal nanoformulations[85] and
343 combination with inhibiting other proteasomal components [86]. Our data suggest that actD could
344 be another way to enhance the effect of BTZ in solid tumors. While we did not observe
345 increased toxicity with this approach in animals, it remains to be seen whether this combination
346 would be tolerated in patients.

347 Compellingly, for our xenograft studies in both KT-53 and 17.94, systemic combination
348 treatment reduced proliferative cells and increased apoptosis. While our *in vitro* experiments
349 test sensitivity over a 72-hour period, *in vivo* experiments more closely model the once-weekly
350 actD dosing used in patients[87]. Our study on KT-53 recapitulated a previously demonstrated
351 insensitivity to actD [51], which we found could be overcome by BTZ. For 17.94, which was
352 sensitive to nanomolar actD concentrations *in vitro*, actD alone was also effective *in vivo*, and

353 adding BTZ produced a small additional effect. The different effects we observed in sensitivity to
354 actD and BTZ suggest that other factors regulating protein homeostasis may also contribute to
355 how cells respond to these drugs. Further studies involving more cell lines, other cancer types,
356 or manipulation of individual factors that regulate protein homeostasis might help explain these
357 differential responses. Together, our findings indicate that the combined use of actD and BTZ
358 could be a promising strategy for combating therapy resistance in anaplastic Wilms tumors.
359 We demonstrated that actD impairs cell cycle progression *in vitro* and *in vivo*, which we
360 attribute to dysregulated proteostasis [15,88,89]. Normally, D-type cyclin levels accumulate in
361 response to mitogenic signaling, promoting the transcription of S-phase genes such as E-type
362 cyclins and chromatin licensing and DNA replication factor 1 (CDT1) [44,90,91]. Consistent with our
363 RPPA in WIT49, we observed in both cell lines that actD reduces Cyclin D2, Cyclin E1, and CDT1
364 levels, suggesting that actD prevents transition to S-phase, when cyclin A is produced. On the
365 other hand, these proteins are normally targeted for proteasomal destruction by the SKP1-
366 CUL1-F-boc protein (SCF) ubiquitin ligase [92], and indeed, we found that BTZ caused them to
367 accumulate. Moreover, BTZ treatment induced apoptosis *in vitro* and *in vivo*, consistent with
368 studies on other cancer cell lines [35-40].
369 In the TARGET cohort [8] , we found that higher levels of proteasome gene expression
370 correlate with anaplastic histology and with poor outcome among some subgroups of relapsed
371 favorable-histology Wilms tumors. Studies across other types of cancer show that the
372 association of proteasome activity with prognosis is context-specific [93]. Lower expression of
373 proteasome subunit genes was associated with reduced survival in head and neck squamous
374 cell carcinoma [94], while studies in breast cancer, glioma, and hepatocellular carcinoma found
375 that higher expression of proteasome subunit genes is associated with worse survival [95-97]. To
376 our knowledge, this is the first study to correlate proteasome expression with worse outcome in
377 Wilms tumor. Anaplastic Wilms tumors are strongly associated with *TP53* mutation [7,8], and
378 *TP53* mutation is known to contribute to proteasome subunit overexpression [98]. To our
379 knowledge, this is the first study to explore the translational landscape of actD treatment in
380 Wilms tumor. Through *in vitro* and *in vivo* models, we propose a model of protein homeostasis-
381 dependent actD sensitivity (Supplementary Figure S10). Use of actD impairs ribosome

382 biogenesis and cell cycle progression while upregulating proteasome activity. Higher
383 proteasome capacity may help Wilms tumor cells escape front-line chemotherapeutics like actD,
384 and this effect may be reversed with proteasome inhibition. Our complementary approaches
385 converged on proteasome activity as a potential mechanism for chemoresistance. Repurposing
386 widely used drugs like BTZ could allow for an accelerated path to clinical translation. More
387 broadly, this strategy could improve treatment not only for Wilms tumor, but also for other
388 tumors where actD is used, such as rhabdomyosarcoma and Ewing sarcoma.
389
390 **Limitations of this study**
391 Our conclusions are limited by the fact that our *in vitro* studies focused on two
392 anaplastic Wilms tumor cell lines, and our *in vivo* studies focused on two anaplastic Wilms
393 tumor PDX lines. We did not compare them to favorable histology Wilms tumor cell lines or
394 xenografts, and we cannot know how our observations might extend to non-anaplastic Wilms
395 tumors. Similarly, our analysis of human Wilms tumor RNA-seq was based on published TARGET
396 data, which only includes rFHWT and DAWT. As such, we do not know whether expression of
397 proteasome components would predict outcome in a population of FHWT at diagnosis.
398 Similarly, as these are retrospective data, the predictive power of these expression patterns
399 needs to be validated in an independent cohort. Lastly, just as *in vitro* findings may vary from *in*
400 *vivo* results, pre-clinical models cannot replace clinical trials. To our knowledge, actD and BTZ
401 have not been given in combination, and the toxicities of such a regimen are unknown.

ACKNOWLEDGMENTS

This work was supported by funds from the Pablove Foundation (to P.D.B.T.); Alex's Lemonade Stand Foundation (to K.S.C.); Cancer Prevention and Research Institute of Texas (RP180805 to L.X., RR180071 to K.S.C.); US Department of Defense (KC220019 to K.S.C.); and National Cancer Institute (K08CA207849 to K.S.C., R21CA259771 and P30CA142543 to L.X., and Cancer Center Support Grant P30CA142543). This research used computational resources provided by the BioHPC supercomputing facility in the Lyda Hill Department of Bioinformatics at UT Southwestern, which is supported by Cancer Prevention and Research Institute of Texas (RP150596). The Functional Proteomics Reverse Phase Protein Array Core was supported in part by The University of Texas MD Anderson Cancer Center, P30CA016672 and R50CA221675. The authors also wish to thank Dr. Philipp Scherer of UT Southwestern Medical Center for use of equipment, Lindsay Mendyka, Lane Beeman, and Chelcea Morris for their technical assistance.

419 **FIGURE LEGENDS**

420

421 **Figure 1. ActD disrupts protein homeostasis in anaplastic Wilms tumor cells**

422 **(A)** Diagram of the effect of actD at the translational level. ActD depletes fully-formed
423 ribosomes and reduces translational capacity. The reduced ribosomes are distributed unevenly.
424 Ribosome profiling provides a snapshot of transcripts actively undergoing translation.

425 **(B)** Whole protein lysates of DMSO (Vehicle) or actD-treated WiT49 or 17.94 fluorescently
426 labeled with AHA-AZDye 680 for nascent protein detection and corresponding loading control
427 TUBULIN detected by western blot from the same gel.

428 **(C,D)** Top 5 most enriched and bottom 5 most depleted KEGG gene sets in ribosome profiling of
429 actD- vs. DMSO-treated WiT49 after 6 hours **(C)** or 72 hours **(D)**.

430 **(E)** GSEA of genome-wide CRISPR knockout screen reveals top 10 most significant KEGG
431 pathways that sensitize WiT49 to actD, ranked by p-value.

432 **(F)** Heatmap displaying RPPA results of actD- vs. DMSO-treated WiT49. Normalized, log2-
433 transformed, median-centered values from validated antibodies with standard deviation over
434 0.1 are shown here.

435

436 **Figure 2. ActD promotes proteasome level and activity in anaplastic Wilms tumor cells**

437 **(A,B)** Western blots for **(A)** and quantification of **(B)** proteasome subunits PSMA6 (α1), PSMB1
438 (β6), PSMB2 (β4), PSMB5 (β5), and PSMD1 (P112), and POMP in WiT49 and 17.94 following 18-,
439 24-, 48-, and 72-hour 2nM actD treatment versus vehicle (DMSO).

440 **(C)** Quantification of relative proteasome-specific chymotrypsin-like activity in WiT49 and 17.94
441 cells following 24 hours of DMSO versus 2nM actD, 8nM BTZ, or 2nM actD + 8nM BTZ
442 treatments (Student's t-test p-value versus vehicle: *<0.05, ** <0.01, ****<0.0001).

443

444 **Figure 3. BTZ sensitizes anaplastic Wilms tumor cell lines to actD *in vitro***

445 **(A)** BTZ kill curves for WiT49 and 17.94 with IC50 values indicated (four-point regression line
446 with shaded region representing 95% confidence interval).

447 **(B)** Heat maps of Loewe synergy scores for combinations of actD and BTZ in WiT49 and 17.94
448 cells.
449 **(C)** Distribution across phases of the cell cycle in WiT49 and 17.94 cells treated with DMSO,
450 actD, BTZ, or combination actD + BTZ for 48 hours. (Student's t-test for treated cells versus
451 DMSO: * <0.05, **<0.01, ***0.001; G0,G1 Phase shown in green, and S Phase in blue).
452 **(D)** Effect of 48-hour treatment WiT49 and 17.94 cells with DMSO, actD, BTZ, and combination
453 actD + BTZ on levels of cell cycle and apoptosis markers by Western blot.
454
455 **Figure 4. BTZ sensitizes subcutaneous anaplastic Wilms tumor xenografts to actD**
456 **(A)** Subcutaneous tumor volumes of NSG mice bearing KT-53 xenografts treated with vehicle,
457 actD, BTZ, and combination actD + BTZ (Student's t-test of endpoint volumes of combination
458 versus vehicle or actD only: * <0.05).
459 **(B)** Kaplan-Meier survival curves for KT-53 tumor-bearing mice treated with vehicle, actD only,
460 BTZ only, and combination (log-rank test versus vehicle ** <0.01)**.**
461 **(C)** Subcutaneous tumor volumes of NSG mice bearing 17.94 xenografts treated with vehicle,
462 actD only, BTZ only, and combination (Student's t-test of endpoint volumes of combination
463 versus vehicle: ***<0.001).
464 **(D)** Kaplan-Meier survival curves for 17.94 tumor-bearing mice treated with vehicle, actD only,
465 BTZ only, and combination.
466 **(E,F)** Quantification of Ki-67 positive nuclei **(E)** and TUNEL positive nuclei **(F)** in in KT-53 and
467 17.94 subcutaneous tumors treated with vehicle, actD only, BTZ only, or combination actD + BTZ
468 (Student's t-test p-value versus vehicle unless otherwise indicated: * <0.05, **<0.01, ***<0.001,
469 ****<0.0001).
470
471 **Figure 5. RNA expression of proteasome genes in TARGET anaplastic histology and relapsed**
472 **favorable histology Wilms tumors**
473 **(A)** Top KEGG pathways enriched in RNA-seq of DAWT versus rFHWT.
474 **(B)** Top reactome pathways enriched in RNA-seq of DAWT versus rFHWT.
475 **(C,D)** Overall survival of Wilms tumor patients stratified according to expression of proteasome

476 enzymatic subunit genes PSMB1, PSMB2, PSMB5 among patients with relapsed favorable

477 histology tumors **(C)** or anaplastic histology tumors **(D)**. (Log Rank test p-value: *<0.05, ** 0.01)

478

479 **STAR METHODS**

480

481 **Experimental Model and Study Details**

482 ***Tissue culture***

483

484 The anaplastic, *TP53*-mutated stage IV Wilms tumor lung metastasis cell line WiT49
485 (RRID: CVCL_0583) from a female patient was maintained in Dulbecco's Modified Eagle Medium
486 (DMEM) with 1000 mg/L glucose, 4 mM L-glutamine, 1 mM pyruvate (Gibco 11995065)
487 supplemented with antibiotic-antimycotic (Gibco 15240062) and fetal bovine serum (Sigma
488 F2442) to 10% final concentration in 37°C at 5% CO_2. A second anaplastic, *TP53*-mutated Wilms
489 tumor cell line 17.94 (Ximbio 153333, RRID:CVCL_D704) originally collected from a female
490 patient was grown in DMEM supplemented with antibiotic-antimycotic and heat inactivated
491 fetal bovine serum (Gibco 16140063) to 20% final concentration in 37°C at 5% CO_2. Cell line
492 identity is annually verified by short tandem repeat (STR) genotyping (last verified November
493 2024). They are also tested biannually for mycoplasma contamination (Latest negative screen
494 November 2024, Lonza LT07-318).

495

496 ***Xenograft tumor models***

497

498 All experiments involving animals were reviewed, approved, and monitored for
499 compliance by the UT Southwestern Institutional Animal Care and Use Committee.
500 To generate xenografts, log growth-phase 17.94 cells or freshly-thawed cryopreserved
501 *TP53* mutated anaplastic Wilms tumor PDX line from a female patient KT-53[51] were injected
502 subcutaneously into the flanks of NOD *scid* gamma (NSG) mice (8-12 weeks at transplantation)
503 in 1 part DPBS and 1 part Matrigel (Corning 354234) at 4 million 17.94 per 100 µl or 1.6 million
504 KT-53 cells per 100 µl per mouse. The mice were then randomized into four anticipated
505 treatment arms, with each sex represented to within n±2 of each other in each treatment
506 group. Tumor growth was measured once a week with calipers in two dimensions. Tumor
507 volume was calculated by dividing the product of the length and the square of the width by 2.

508 Upon reaching the thresholds of 150 mm^3 for 17.94 and 100 mm^3 for KT-53, mice were began
509 one of four treatments: actD only, BTZ only, both actD + BTZ and vehicle. Mice in the actD only
510 and actD+BTZ arms were dosed with actD (in 2.5% DMSO, 40% PEG300, 5% Tween-80, 52.5%
511 saline) once a week intraperitoneally (0.2 mg/kg for 17.94, 0.15 mg/kg for KT-53). Mice in the
512 BTZ only or actD+BTZ arms were dosed with BTZ (in 0.5% DMSO, 30% PEG300, 69.5% distilled
513 deionized water) once a week intravenously (0.2mg/kg). Mice in the vehicle arm received both
514 solvents once a week. Treatment continued until tumor volumes reached 1,500 mm^3 or at
515 maximum 8 weeks for KT-53 and 12 weeks for 17.94 post first dose—conditions at which all but
516 actD+BTZ, or DMSO and BTZ respectively are either already terminated or at least 1,000 mm^3.
517 At the end of therapy, tumors were harvested for histological processing. Statistical analyses for
518 tumor volume were performed by two-tailed Student's T-test for each pairwise comparison
519 between the four treatment arms. Kaplan-Meier survival curves were compared between each
520 group by log-rank test.
521
522 **Method Details**
523
524 ***Ribosomal RNA quantification***
525
526 To determine the effect of actD on rRNA expression, WiT49 or 17.94 cells were seeded at
527 ~50% confluency in 3 different plates. The following day, cells were treated with either vehicle
528 (DMSO) or 2nM actD for 6 hours or 24 hours. At experiment endpoint, total RNA was extracted
529 using the miRNeasy kit with DNase I digestion (Qiagen 217004 and 79254), and cDNA synthesis
530 was performed with iScript™ Reverse Transcription Supermix (Bio-Rad 1708841). Quantitative
531 PCR (qPCR) was performed in four technical replicates per condition using iTaq™ Universal
532 SYBR® Green Supermix (Bio-Rad 1725125) with primers listed: *18s* rRNA
533 (GTAACCCGTTGAACCCCATT, CCATCCAATCGGTAGTAGCG); *45s* pre-rRNA (ACCCACCCTCGGTGAGA,
534 CAAGGCACGCCTCTCAGAT); *GAPDH* (CGGAGTCAACGGATTTGGT, ACCAGAGTTAAAAGCAGCCC).
535 Relative expression was calculated by the $2^{-\Delta\Delta Ct}$ method by normalizing each rRNA species to

536 *GAPDH*. Significance was determined by unpaired two-tailed Student's T-test versus vehicle
537 control. A second biological replicate was performed as above to confirm the results.
538
539 ***Protein synthesis quantification***
540
541 To determine the effect of actD on protein synthesis using Click-iT® AHA (L-
542 azidohomoalanine, Invitrogen C10102), WiT49 or 17.94 cells were first seeded at 30%
543 confluency in 15 cm plates and treated the following day with 2nM actD or DMSO in complete
544 media. Following 48 hours of drug exposure, the media was replaced with methionine-free
545 complete media [DMEM without methionine (Gibco 21013024), with 10% dialyzed FBS (Gibco
546 A3382001), 1x antibiotic-antimycotic (Gibco 15240062), 0.2 mM L-Cystine (Thermo Scientific
547 J61651.09), 4mM L-Glutamine (Gibco 25030149), 1mM Sodium Pyruvate (Gibco 11360070)]
548 containing DMSO or 2nM actD for 30 minutes to wash out any residual methionine. After 30
549 minutes in methionine-free media, the media was supplemented with Click-iT® AHA to a final
550 concentration of 50µM, and the cells were returned to the incubator for 4 hours. Whole protein
551 lysates were extracted from these cells with RIPA buffer (Sigma R0278), supplemented with
552 protease and phosphatase inhibitors (Invitrogen A32961), sonicated, and quantified by BCA
553 protein assay (Thermo Scientific 23227). For AHA-detection, we used the Click-&-Go® Click
554 Chemistry Reaction Buffer Kit (Vector Laboratories Inc. CCT-1001) with AZDye 680 Alkyne
555 (Vector Laboratories Inc. CCT-1001) according to manufacturer recommendations. For each
556 condition, 20µg of total protein lysates were reacted with the alkyne reagent at a final
557 concentration of 20µM. Following denaturing SDS-PAGE, the gel was imaged (LI-COR Biotech) to
558 detect proteins with AZDye 680 conjugated AHA. Results were performed with biological
559 replicates to confirm reproducibility.
560 Additionally, we detected nascent protein synthesis using O-propargyl-puromycin (OPP)
561 incorporation. WiT49 cells were seeded at ~30% confluency in cell culture chamber slides. The
562 following day, cells were treated with either vehicle (DMSO) or 2nM actD for 48 hours or 72
563 hours. At the endpoint, protein synthesis was measured using a fluorescence-based O-
564 propargyl-puromycin (OPP) incorporation kit (Invitrogen C10457) according to manufacturer

565 protocols. Nuclei were counterstained with DAPI (4',6-diamidino-2-phenylindole). Each
566 condition was photographed at 5 non-overlapping regions at 20x magnification on a BZ-X810
567 Fluorescence microscope (Keyence Corporation) and quantified using Fiji [99]. Necrotic regions
568 were disregarded. Relative fluorescence units were calculated from the blue (DAPI) and red
569 (OPP-Alexa Fluor 488) channels. The number of nuclei was counted from the DAPI channel using
570 the Watershed and Analyze Particles functions in Fiji. Raw protein synthesis was calculated as
571 the average red fluorescence intensity in pixels with any fluorescence using the Area and
572 Integrated Density functions in Fiji. For each image, raw protein synthesis was then normalized
573 to the number of nuclei in that field of view. Each field of view was treated as a technical
574 replicate, and statistical analysis was performed by unpaired two-tailed Student's t-test against
575 untreated cells.
576
577 ***Reverse phase protein array***
578
579 WiT49 cells at 20% density were treated with 1 nM actD or DMSO as vehicle control for
580 72 hours in duplicate. 1×10^6 cells were collected, washed, and frozen in liquid nitrogen, and sent
581 to the MD Anderson Functional Proteomic Reverse Phase Protein Array Core [100-102]. Normalized,
582 log2-transformed, median-centered values from "validated" antibodies were used for analysis
583 [103]. The log2-fold-change for each antibody was calculated as the difference between the means
584 of actD-treated and DMSO-treated samples, and the standard deviation for each antibody was
585 calculated as the standard deviation of all four values.
586
587 ***Ribosome profiling***
588
589 WiT49 cells were incubated in complete growth medium with 2nM actD or DMSO for 6
590 or 72 hours, in three technical replicate plates per condition. For 2-week long treatments,
591 WiT49 were maintained and passaged in two 7-day cycles of drug/vehicle-supplemented media
592 for 3 days, followed by drug-free complete growth media for 4 days, three technical replicate
593 plates per condition.

594 1.5×10^7 cells were used for each replicate for ribosome sequencing. Ribosome
595 footprints were isolated based on previous publications [104,105], and each RNA sample was spiked
596 with 24 fmol of the synthetic 28-nt RNA oligo 5'-AUGUAACACGGAGUCGACCCGCAACGCGA-3' [106].
597 rRNA depletion was performed using the Low Input RiboMinus™ Eukaryote System v2 (Thermo
598 Fisher A15027), and sequencing libraries were generated using the NEBNext® Small RNA Library
599 Prep Set for Illumina® (NEB E7330). Libraries were pooled and sequenced using NextSeq 500
600 High Output, single-end reads, 75 cycles. In parallel, RNA was extracted for total RNA
601 sequencing using the Direct-zol RNA Miniprep Kit (ZymoResearch R2050) or the miRneasy Mini
602 Kit (Qiagen 217004) according to manufacturer protocols, followed by rRNA depletion as above
603 and DNase-treatment. Sequencing libraries were prepared with the TruSeq Stranded Total RNA-
604 seq Sample Prep Kit from Illumina and sequenced paired-end for 6-hour and 72-hr, and single-
605 end for 14-day time points.
606 Trimmed reads from ribosome profiling and RNA sequencing were aligned to the hg38
607 reference genome using HISAT2 [107]. For ribosome profiling, reads longer than 30 nucleotides
608 were filtered out, and remaining reads were assembled to GENCODE v26 transcript annotations
609 using StringTie [108]. Ribosome profiling quantifications were normalized to mapped spike-in
610 reads, and RNA-seq reads were normalized to million mapped reads. Translational efficiency
611 (TE) for each gene was calculated by dividing the number of normalized ribosome footprint
612 reads by the number of normalized RNA sequencing reads. Differential TE was calculated using
613 t-tests on log2-transformed TE of three actD-treated technical replicates versus three DMSO-
614 treated technical replicates. Geneset enrichment analysis (GSEA) was performed using the fgsea
615 package (v1.26.0) on log2-fold change of TE using gene sets from MSigDB v7.1 [17,109-111].
616
617 ***CRISPR screen***
618
619 The CRISPR knock-out screen was performed on WiT49 cells using the Human Brunello
620 CRISPR knockout pooled library, a gift from David Root and John Doench (Addgene 73178). The
621 plasmid library was propagated, verified for maintenance of representation, and transfected as
622 recommended [112]. The viral supernatant was transduced into 1.0×10^8 WiT49 cells, at

623 multiplicity of infection of 0.3. Forty-eight hours after transduction, the cells were selected with
624 0.5 µg/ml puromycin for 7 days. After selection, 3×10^7 transduced cells were collected as
625 transduction reference, and the rest were split into four dishes, two per treatment condition.
626 These remaining cells were expanded and treated with either 2nM actD or DMSO for 4 days.
627 The media was then replaced in both conditions for a washout of 3 days without actD or DMSO.
628 Following this, another 7-day cycle (4 days actD or DMSO treatment followed by 3 days
629 washout) was carried out. Finally, genomic DNA was extracted using DNeasy Blood & Tissue Kit
630 (Qiagen 69506), and a sequencing library was prepared from genomically-integrated single
631 guide RNA (sgRNA) sequences by PCR using barcoding and staggered primer pairs as in
632 Supplementary Table S7 [112]. These were gel-size selected and sequenced at ~2.4 million single-
633 end reads each, 100-bp length.
634 Computational analysis of CRISPR screens was performed using the MAGeCKFlute
635 pipeline following published guidelines [113]. In brief, we mapped reads using the command
636 'mageck count', and we tested sgRNA knockout efficiency using the command 'mageck mle'.
637 Downstream analysis was performed using the FluteRRA function in the MAGeCKFlute R
638 package, with the 'mageck mle' output file as the input. To perform KEGG pathway enrichment
639 analysis, the 'mageck pathway' command was used with the KEGG gene set from the Molecular
640 Signatures Database (v7.1) [109]. [113,114]
641
642 ***Western blot***
643
644 For the actD timecourse, WiT49 or 17.94 was seeded at ~30% confluency overnight. The
645 following day, without replacing the media, actD (or an equivalent volume of DMSO) was spiked
646 into the media to a final concentration of 2 nM, for 72-hour treatment. The next day, another
647 plate of WiT49 or 17.94 began 48-hour treatment with 2nM actD. We repeated this the
648 following day for the 24-hour treatment and 18-hour treatments. Upon completion of the
649 allotted incubation times, we collected cells for protein lysate extraction. For actD and BTZ *in*
650 *vitro* drug treatments, we seeded WiT49 or 17.94 at 20-30% confluency overnight. We then
651 treated cells with either 2nM actD alone, 8nM BTZ alone, 2nM actD + 8nM BTZ, or DMSO at

652 equivalent volume without changing media. After 48 hours of drug exposure, cells were
653 collected for protein lysate extraction.
654 Protein lysates were extracted from flash-frozen pellets with RIPA buffer (Sigma R0278),
655 supplemented with protease and phosphatase inhibitors (Invitrogen A32961), sonicated, and
656 quantified by BCA protein assay (Thermo Scientific 23227). Following denaturing SDS-PAGE and
657 transfer to PVDF or nitrocellulose membranes, blots were blocked with 5% bovine serum
658 albumin in tris-buffered saline with Tween-20. Primary antibodies used are as follows and were
659 diluted to 1:3,000 unless otherwise stated: Tubulin (Cell Signaling Technology 3873,
660 RRID:AB_1904178), GAPDH (Cell Signaling Technology 97166, RRID:AB_2756824), Caspase-7
661 (Cell Signaling Technology 12827, RRID:AB_2687912), cleaved Caspase-7 (Cell Signaling
662 Technology 8438, RRID:AB_11178377; 1:1,000), Cyclin D2 (Cell Signaling Technology 3741;
663 RRID:AB_2070685), CDT1 (Cell Signaling Technology 8064, RRID:AB_10896851), Cyclin E1 Cell
664 Signaling Technology 20808, RRID:AB_2783554), Cyclin A2 (Cell Signaling Technology
665 91500RRID:AB_3096041), PARP (Cell Signaling Technology 9532, RRID:AB_659884), cleaved
666 PARP (Cell Signaling Technology 5625, RRID:AB_10699459; 1:1,000), POMP (Cell Signaling
667 Technology 15141, RRID:AB_2798726), PSMA6 (Cell Signaling Technology 2459,
668 RRID:AB_2268879), PSMB1 (Invitrogen PA5-49648, RRID: AB_2635102; 1:5,000), PSMB2
669 (Proteintech 15154-1-AP, RRID:AB_2300322; 1:5,000), PSMB5 (Cell Signaling Technology 12919,
670 RRID:AB_2798061; 1:5,000), PSMD1 (Sigma SAB2104781, RRID:AB_10668741), RPL5 (Cell
671 Signaling Techonology 51345, RRID:AB_2799391), RPL7 (abcam ab72550, RRID:AB_1270391),
672 RPL11 (Cell Signaling Technology 18163, RRID:AB_2798794), RPL26 (Cell Signaling Technology
673 2065, RRID:AB_2146242), Total AKT (Cell Signaling Technology 9272, RRID:AB_329827),
674 Phospho-AKT (Ser473) (Cell Signaling Technology 4060, RRID:AB_2315049; 1:1,000), Total 4E-
675 BP1 (Cell Signaling Technology 9452, RRID:AB_331692), Phospho-4E-BP1 (Thr37/46) (Cell
676 Signaling Technology 2855, RRID:AB_560835; 1:1,000), Total P70-S6K1 (Cell Signaling
677 Technology 34475, RRID:AB_2943679), and Phospho- P70-S6K1 (Thr389) (Invitrogen 710095,
678 AB_2532559; 1:1,000). HRP-conjugated secondary antibodies used are Anti-Mouse IgG (Cell
679 Signaling Technology 7076, RRID:AB_330924; 1:10,000) or Anti-Rabbit IgG (Cell Signaling

680 Technology 7074, RRID:AB_2099233; 1:5,000). Each western blot run was performed at
681 minimum with a second biological replicate, and band intensities were quantified using Fiji [115].
682
683 ***In vitro drug inhibition***
684
685 To quantify drug inhibitory activity, 1,000 cells per well were seeded in black-walled 96-
686 well plates at 100 µl/well. The following day, serial dilutions of actD (Sigma A1410), BTZ (Sigma
687 5043140001), or Rapamycin (Selleckchem S1039) were added in 3 technical replicate wells per
688 dose. Vehicle control was also included to yield equivalent final concentrations of DMSO (<0.1%)
689 in all wells. For synergy determination experiments, each drug of interest was serially diluted
690 alone and then mixed into a range of combinations. Each dose was then added onto the cells in
691 triplicate. After 72 hours, cell density was assayed by adding 20 µL 0.15 mg/ml resazurin in
692 phosphate-buffered saline in each well, including cell-free wells as background controls and
693 drug-free wells as normalization controls. After 1-4 hours at 37°C, fluorescence was measured
694 using a microplate reader with excitation set at 550 nm and emission at 590 nm. Combination
695 treatment effects were determined using the Loewe synergy model dose-response calculation
696 and 95% confidence interval determination through Synergyfinder+ [116]. Each experimental
697 condition with three technical replicates was repeated at least twice to confirm reproducibility
698 of outcomes.
699
700 ***Proteasome activity assay***
701
702 To measure proteasome enzymatic activity, we seeded 1,000 cells per well concurrently
703 in duplicate 96-well plates: one black-walled (for quantifying cell density) and one white-walled
704 (for quantifying proteasome activity). The following day, cells were treated with each of the
705 following conditions in quadruplicate with identical conditions in both plates: 2nM actD, 2 nM
706 actD + 1 mM MG-132 (Selleckchem S2619), 8 nM BTZ, 8 nM + 1 mM MG-132, DMSO, or DMSO +
707 1 mM MG-132. Each condition was performed with or without MG-132 to correct for the level
708 of non-proteasome chymotrypsin-like activity. Wells without cells were used as background

709 controls. After 48 hours, the black-walled plate was used to determine cell viability using
710 resazurin as described above, and the white-walled plate was used to quantify proteasome
711 enzymatic activity. We used Proteasome-Glo™ Chymotrypsin-like Assay (Promega G8621) and
712 calculated the proteasome enzymatic activity in accordance with manufacturer
713 recommendations. Briefly, after subtracting background controls, we normalized each condition
714 to viability based on the corresponding wells in the black-walled plate to account for differences
715 in cell density. We then subtracted the normalized luminescence of each condition with MG-132
716 from the corresponding wells without MG-132 to yield the viability-normalized luminescence
717 attributable to proteasome activity. Statistical significance was calculated between treatment
718 conditions using unpaired, two-tailed Student's T-test. The assay repeated at least twice for
719 both cell lines to confirm reproducibility of outcomes.
720
721 ***Cell Cycle Phase Determination***
722
723 To characterize the cell cycle phase distribution of WiT49 or 17.94 following drug
724 treatment, we used flow cytometry with propidium iodide (Invitrogen F10797) with EdU
725 (Invitrogen C10636) according to manufacturer recommendations. In detail, WiT49 or 17.94
726 cells were seeded at 30% confluency in 6-well plates. To perform cell cycle synchronization, the
727 media in all but one (asynchronous control) well was replaced with DMEM (Gibco 11995065)
728 with antibiotic-antimycotic (Gibco 15240062) and fetal bovine serum (Sigma F2442) at a
729 reduced concentration of 0.2%. After a 24-hour incubation at 37°C at 5% CO_2, the media was
730 replaced with complete media with the full concentration of serum (10% for WiT49 and 20% for
731 17.94), with either 2nM actD, 8nM BTZ, 2nM actD + 8nM BTZ, or DMSO. After 48 hours of drug
732 exposure, EdU (Invitrogen C10636) was added to each well, to a final concentration of 10µM,
733 for 2 hours. The cells were gently dissociated , washed, fixed, and permeabilized in preparation
734 for flow cytometry analysis according to the manufacturer protocols. The stained cells were
735 resuspended in propidium iodide staining solution (Invitrogen F10797) for at least 15 minutes at
736 room temperature and were analyzed by flow cytometry BD FACSCAnto (BD Life Sciences). The
737 results were analyzed using FlowJo (BD Life Sciences). Populations in each cell cycle phase were

obtained in triplicate runs and compared by Student's T-test against the cell cycle phase proportions of the DMSO condition.

IHC & TUNEL

Two representative samples from each treatment arm were formalin-fixed, paraffin-embedded, and sectioned at 4 µm thickness. These were used for immunohistochemistry (IHC) and TUNEL assay.

For IHC, antibodies used were Ki-67 (Abcam ab15580, RRID:AB_443209, 1:1,000 for primary) with anti-Rabbit HRP (Vector Laboratories Inc. MP-7451, RRID:AB_2631198 for secondary). Each slide was photographed in at least four distinct 40x magnified fields of view (Keyence Corporation). Numbers of total nuclei and DAB-positive nuclei in each field were quantified using Fiji [115]. Non-tumor regions were omitted from quantification. Statistical analysis was performed by unpaired two-tailed Student's t-test between each pair of treatment arms.

To measure apoptosis in tumor sections, we used Click-iT™ Plus TUNEL Assay kit (Invitrogen C10617) according to the manufacturer recommendations and counterstained nuclei with DAPI. Each tissue slide was photographed in at least four distinct 40x magnified fields of view (Keyence Corporation). Numbers of total nuclei and TUNEL-positive nuclei and quantified using Fiji [115]. Non-tumor regions were omitted from quantification. Statistical analysis was performed by unpaired two-tailed Student's t-test between each pair of treatment arms.

TARGET database reanalysis

Tables of Wilms tumor RNA-seq counts and clinical annotation were downloaded from the NCI TARGET[8] website on May 21, 2019. Protein-coding genes were identified based on ENSEMBL v86 annotations. Differential expression analysis for DAWT versus FHWT was performed with DESeq2 (v1.40.2), followed by gene set enrichment analysis using fgsea (v1.26.0) based on MSigDB v7.1 gene sets [17,111,117].

766 We compared outcomes for these patients according to expression of proteasome
767 enzymatic subunits in cBioportal [52,53]. Specifically, we obtained RNA-seq RPKM z-scores for
768 *PSMB5*, *PSMB6*, and *PSMB7,* compared to tumors that are diploid for that gene. For patients
769 with multiple samples, the primary tumor sample was used. Log-rank tests were used to
770 compare survival curves.
771
772 ***Data availability***
773
774 Ribosome profiling and accompanying RNA-seq data from WiT49 are deposited in the
775 NCBI GEO database under accession GSE270330.
776
777
778 **Statistical Analysis**
779
780 Statistical analyses, standard error, or 95% confidence intervals for the above were performed
781 with the aid of GraphPad Prism software unless otherwise indicated, and details of each test
782 used are referenced in figure legends. All data with replicates are presented as mean and error
783 bars shown are for standard error of the mean. Values of $p < 0.05$ are considered statistically
784 significant.

785 **SUPPLEMENTARY FIGURES**

786

787 **Supplementary Figure S1. ActD alters global translation in WiT49 anaplastic Wilms tumor cells**

788 **(A)** ActD kill curves for anaplastic Wilms Tumor cell lines WiT49 and 17.94 with IC50 values

789 indicated (four-point regression line with shaded region representing 95% confidence interval).

790 **(B)** Levels of 45s pre-rRNA and 18s mature rRNA in anaplastic Wilms tumor cell lines WiT49 and

791 17.94, quantified by qPCR following actD treatment for 6 and 24 hours.

792 **(C,D)** Micrographs **(C)** and quantification **(D)** of protein synthesis assay. Red fluorescence

793 measures O-propargyl-puromycin (OPP) incorporation relative to total area of WiT49 cells

794 treated with 48 and 72 hours of 2nM actD or vehicle DMSO. (Student's t-test vs. vehicle, **

795 $p<0.01$.)

796

797 **Supplementary Figure S2. Ribosome footprints are depleted at translation initiation sites in**

798 **actD-treated WiT49.**

799 **(A-F)** Proportion of left edge of ribosome footprints (y-axis) relative to translation initiation site

800 (0 on x-axis), on the top 30% most abundant transcripts, in samples treated with DMSO **(A-C)** or

801 actD **(D-F)** at 72 hours. Peak position highlighted in red.

802

803 **Supplementary Figure S3. Ribosome profiling metrics in actD-treated WiT49.**

804 **(A,B)** Log2-transformed counts aligning to each gene, by RNA-seq **(A)** and translation efficiency

805 by ribosome profiling **(B)** after 6-hour, 72-hour, and 2-week treatments of WiT49 with actD

806 (y-axes) versus DMSO (x-axes).

807

808 **Supplementary Figure S4. ActD induces translation of ribosome and proteasome subunits and**

809 **upregulates Akt/mTOR signaling.**

810 **(A,B)** KEGG_ RIBOSOME pathway enrichment plots after 6 hours **(A)** and 72 hours **(B)** of actD vs.

811 DMSO. NES, normalized enrichment score.

812 **(C)** KEGG_RIBOSOME gene set enrichment plot for RNA expression after 72 hours of actD vs.

813 DMSO.

814 **(D,E)** KEGG_ PROTEASOME pathway enrichment plots after 6 hours **(D)** and 72 hours **(E)** of actD
815 vs. DMSO.
816 **(F)** KEGG_PROTEASOME gene set enrichment plot for RNA expression after 72 hours of actD vs.
817 DMSO.
818 **(G,H)** Phosphorylation of Akt/mTOR signaling components visualized and quantified by Western
819 blot in WiT49 and 17.94 following 2nM actD.
820 **(I)** Rapamycin kill curves for anaplastic Wilms tumor cell lines WiT49 and 17.94 (four-point
821 regression line with shaded region representing 95% confidence interval).
822 **(J)** Heat maps of Loewe synergy scores for combinations of actD and rapamycin in WiT49 and
823 17.94 cells.
824
825 **Supplementary Figure S5. ActD and BTZ affect ribosomal protein levels.**
826 **(A)** Western blots for and quantification of **(B)** ribosomal protein subunits RPL5, RPL7, RPL11,
827 and RPL26 in WiT49 and 17.94 following 48-hour treatment of DMSO, 2nM actD, 8nM BTZ, or
828 2nM actD + 8nM BTZ.
829
830 **Supplementary Figure S6. Body weight changes in mice treated with actD, BTZ, or**
831 **combination.**
832 **(A,B)** Relative body weight of mice bearing KT-53 xenografts **(A)** or 17.94 xenografts **(B)**, during
833 treatment with actD, BTZ, or both.
834
835 **Supplementary Figure S7. Bortezomib enhances cytotoxicity of actinomycin D in anaplastic**
836 **Wilms tumor xenografts.**
837 **(A,B)** Low-power and high-power H&E images of **(A)** KT-53 and **(B)** 17.94 subcutaneous tumors
838 (Black bar = 1.0 mm; Blue Bar =100 µm)
839 **(C, D)** High-power photomicrographs of Ki-67 immunohistochemistry of KT-53 (Bar =100 µm) **(C)**
840 and 17.94 **(D)**.
841 **(E, F)** High-power photomicrographs of TUNEL stain of KT-53 (Bar =100 µm) **(E)** and 17.94 **(F)**.
842

843 **Supplementary Figure S8. Enrichment for proteasome gene sets in anaplastic Wilms tumor.**
844 **(A,B)** GSEA plot showing enrichment for KEGG_PROTEASOME **(A)** and
845 REACTOME_APC_C_MEDIATED_DEGRADATION_OF_CELL_CYCLE_PROTEINS **(B)** in anaplastic
846 Wilms tumor vs. relapsed favorable-histology Wilms tumors in TARGET dataset.
847
848 **Supplementary Figure S9. Survival of relapsed favorable histology Wilms tumor (FHWT) by**
849 **stage and proteasome expression.**
850 **(A)** Overall survival of all relapsed FHWT in TARGET, stratified according to expression of
851 proteasome enzymatic subunit genes *PSMB1*, *PSMB2*, *PSMB5*. **(B-E)** Overall survival of relapsed
852 FHWT in TARGET, for Stages I, II, III, and IV at diagnosis, stratified according to expression of
853 proteasome enzymatic subunit genes *PSMB1*, *PSMB2*, *PSMB5*. (Log rank test p-value: *<0.05, **
854 < 0.01, *** 0.001).
855
856 **Supplementary Figure S10. Model for effect of actinomycin D on protein homeostasis in**
857 **Wilms tumor cells.**
858

859 **SUPPLEMENTARY TABLES**

860

861 **Supplementary Table S1.** Average log2-transformed translational efficiency for WiT49 in 6-hour
862 and 72-hour actD versus DMSO treatments derived from ribosome profiling sequencing.
863 **Supplementary Table S2.** GSEA of translationally enriched KEGG pathways for WiT49 6-hour and
864 72-hour actD versus DMSO treatments from ribosome profiling sequencing.

865

866 **Supplementary Table S3.** KEGG pathway enrichment summary table from Mageck-Flute
867 pathway output.

868

869 **Supplementary Table S4.** Normalized, log2-transformed, median-centered RPPA values of
870 validated antibodies from WiT49 cells treated with actD or DMSO.

871

872 **Supplementary Table S5.** Loewe synergy scores (and 95% confidence interval) for actD with BTZ
873 or rapamycin, in WiT49 or 17.94.

874

875 **Supplementary Table S6.** GSEA of enriched KEGG and Reactome pathways in DAWT versus
876 FHWT.

877

878 **Supplementary Table S7.** List of oligonucleotides used in this study

879

880 **REFERENCES**
881
882
883

884 1 Howlader N, N. A., Krapcho M, Miller D, Brest A, Yu M, Ruhl J, Tatalovich Z, Mariotto A,
885 Lewis DR, Chen HS, Feuer EJ, Cronin KA (eds). . *SEER Cancer Statistics Review, 1975-2018,*
886 *National Cancer Institute*, <https://seer.cancer.gov/csr/1975_2018/, > (2018).
887 2 Termuhlen, A. M. *et al.* Twenty-five year follow-up of childhood Wilms tumor: a report
888 from the Childhood Cancer Survivor Study. *Pediatr Blood Cancer* **57**, 1210-1216 (2011).
889 https://doi.org:10.1002/pbc.23090
890 3 Ehrlich, P. *et al.* Results of the First Prospective Multi-institutional Treatment Study in
891 Children With Bilateral Wilms Tumor (AREN0534): A Report From the Children's
892 Oncology Group. *Ann Surg* **266**, 470-478 (2017).
893 https://doi.org:10.1097/SLA.0000000000002356
894 4 Groenendijk, A. *et al.* Prognostic Factors for Wilms Tumor Recurrence: A Review of the
895 Literature. *Cancers (Basel)* **13** (2021). https://doi.org:10.3390/cancers13133142
896 5 Brok, J. *et al.* Unmet needs for relapsed or refractory Wilms tumour: Mapping the
897 molecular features, exploring organoids and designing early phase trials - A collaborative
898 SIOP-RTSG, COG and ITCC session at the first SIOPE meeting. *Eur J Cancer* **144**, 113-122
899 (2021). https://doi.org:10.1016/j.ejca.2020.11.012
900 6 Daw, N. C. *et al.* Activity of Vincristine and Irinotecan in Diffuse Anaplastic Wilms Tumor
901 and Therapy Outcomes of Stage II to IV Disease: Results of the Children's Oncology
902 Group AREN0321 Study. *Journal of clinical oncology : official journal of the American*
903 *Society of Clinical Oncology* **38**, 1558-1568 (2020). https://doi.org:10.1200/JCO.19.01265
904 7 Ooms, A. H. *et al.* Significance of TP53 Mutation in Wilms Tumors with Diffuse Anaplasia:
905 A Report from the Children's Oncology Group. *Clinical cancer research : an official*
906 *journal of the American Association for Cancer Research* **22**, 5582-5591 (2016).
907 https://doi.org:10.1158/1078-0432.CCR-16-0985
908 8 Gadd, S. *et al.* A Children's Oncology Group and TARGET initiative exploring the genetic
909 landscape of Wilms tumor. *Nature genetics* **49**, 1487-1494 (2017).
910 https://doi.org:10.1038/ng.3940
911 9 Macmahon, H. E., Bedizel, M. & Ellis, C. A. Vincristine (Leurocristine) Sulfate in the
912 Treatment of Children with Metastatic Wilms' Tumor. Pediatric Division, Southwest
913 Cancer Chemotherapy Group. *Pediatrics* **32**, 880-887 (1963).
914 10 Windmiller, J., Berry, D. H., Haddy, T. B., Vietti, T. J. & Sutow, W. W. Vincristine sulfate in
915 the treatment of neuroblastoma in children. *Am J Dis Child* **111**, 75-78 (1966).
916 https://doi.org:10.1001/archpedi.1966.02090040111014
917 11 Gaspar, N. *et al.* Ewing Sarcoma: Current Management and Future Approaches Through
918 Collaboration. *Journal of clinical oncology : official journal of the American Society of*
919 *Clinical Oncology* **33**, 3036-3046 (2015). https://doi.org:10.1200/JCO.2014.59.5256
920 12 Miwa, S. *et al.* Recent Advances and Challenges in the Treatment of
921 Rhabdomyosarcoma. *Cancers (Basel)* **12** (2020).
922 https://doi.org:10.3390/cancers12071758

13 D'Angio, G. J. The National Wilms Tumor Study: a 40 year perspective. *Lifetime Data Anal* **13**, 463-470 (2007). https://doi.org:10.1007/s10985-007-9062-0

14 Veal, G. J. *et al.* Pharmacokinetics of dactinomycin in a pediatric patient population: a United Kingdom Children's Cancer Study Group Study. *Clinical cancer research : an official journal of the American Association for Cancer Research* **11**, 5893-5899 (2005). https://doi.org:10.1158/1078-0432.CCR-04-2546

15 Walsh, C. *et al.* Development of a physiologically based pharmacokinetic model of actinomycin D in children with cancer. *Br J Clin Pharmacol* **81**, 989-998 (2016). https://doi.org:10.1111/bcp.12878

16 Perry, R. P. Selective effects of actinomycin D on the intracellular distribution of RNA synthesis in tissue culture cells. *Experimental Cell Research* **29**, 400-406 (1963).

17 Subramanian, A. *et al.* Gene set enrichment analysis: a knowledge-based approach for interpreting genome-wide expression profiles. *Proc Natl Acad Sci U S A* **102**, 15545-15550 (2005). https://doi.org:10.1073/pnas.0506580102

18 Schöfer, C., Weipoltshammer, K., Almeder, M., Muller, M. & Wachtler, F. Redistribution of ribosomal DNA after blocking of transcription induced by actinomycin D. *Chromosome Res* **4**, 384-391 (1996). https://doi.org:10.1007/BF02257274

19 Mills, E. W. & Green, R. Ribosomopathies: There's strength in numbers. *Science* **358** (2017). https://doi.org:10.1126/science.aan2755

20 Ingolia, N. T., Ghaemmaghami, S., Newman, J. R. & Weissman, J. S. Genome-wide analysis in vivo of translation with nucleotide resolution using ribosome profiling. *Science* **324**, 218-223 (2009). https://doi.org:10.1126/science.1168978

21 Ingolia, N. T. Ribosome profiling: new views of translation, from single codons to genome scale. *Nat Rev Genet* **15**, 205-213 (2014). https://doi.org:10.1038/nrg3645

22 Lam, Y. W., Lamond, A. I., Mann, M. & Andersen, J. S. Analysis of nucleolar protein dynamics reveals the nuclear degradation of ribosomal proteins. *Curr Biol* **17**, 749-760 (2007). https://doi.org:10.1016/j.cub.2007.03.064

23 Liu, R. *et al.* Impairing the production of ribosomal RNA activates mammalian target of rapamycin complex 1 signalling and downstream translation factors. *Nucleic Acids Res* **42**, 5083-5096 (2014). https://doi.org:10.1093/nar/gku130

24 Huang, C. C. *et al.* Predicting relapse in favorable histology Wilms tumor using gene expression analysis: a report from the Renal Tumor Committee of the Children's Oncology Group. *Clinical cancer research : an official journal of the American Association for Cancer Research* **15**, 1770-1778 (2009). https://doi.org:10.1158/1078-0432.CCR-08-1030

25 Flores, L. G., 2nd *et al.* Monitoring therapy with MEK inhibitor U0126 in a novel Wilms tumor model in Wt1 knockout Igf2 transgenic mice using 18F-FDG PET with dual-contrast enhanced CT and MRI: early metabolic response without inhibition of tumor growth. *Mol Imaging Biol* **15**, 175-185 (2013). https://doi.org:10.1007/s11307-012-0588-5

26 Kahan, B. D. *et al.* Therapeutic drug monitoring of sirolimus: correlations with efficacy and toxicity. *Clin Transplant* **14**, 97-109 (2000). https://doi.org:10.1034/j.1399-0012.2000.140201.x

27 Iadevaia, V., Liu, R. & Proud, C. G. mTORC1 signaling controls multiple steps in ribosome biogenesis. *Semin Cell Dev Biol* **36**, 113-120 (2014). https://doi.org:10.1016/j.semcdb.2014.08.004

28 Sung, M. K. *et al.* A conserved quality-control pathway that mediates degradation of unassembled ribosomal proteins. *Elife* **5** (2016). https://doi.org:10.7554/eLife.19105

29 Sung, M. K., Reitsma, J. M., Sweredoski, M. J., Hess, S. & Deshaies, R. J. Ribosomal proteins produced in excess are degraded by the ubiquitin-proteasome system. *Mol Biol Cell* **27**, 2642-2652 (2016). https://doi.org:10.1091/mbc.E16-05-0290

30 Hanley, M. J. *et al.* Population Pharmacokinetic Analysis of Bortezomib in Pediatric Leukemia Patients: Model-Based Support for Body Surface Area-Based Dosing Over the 2- to 16-Year Age Range. *J Clin Pharmacol* **57**, 1183-1193 (2017). https://doi.org:10.1002/jcph.906

31 Moreau, P. *et al.* Pharmacokinetic, pharmacodynamic and covariate analysis of subcutaneous versus intravenous administration of bortezomib in patients with relapsed multiple myeloma. *Clin Pharmacokinet* **51**, 823-829 (2012). https://doi.org:10.1007/s40262-012-0010-0

32 Adams, J. *et al.* Proteasome inhibitors: a novel class of potent and effective antitumor agents. *Cancer Res* **59**, 2615-2622 (1999).

33 Wu, M. H. & Yung, B. Y. Cell cycle phase-dependent cytotoxicity of actinomycin D in HeLa cells. *Eur J Pharmacol* **270**, 203-212 (1994). https://doi.org:10.1016/0926-6917(94)90064-7

34 Kim, H. K. *et al.* Investigation of cell cycle arrest effects of actinomycin D at G1 phase using proteomic methods in B104-1-1 cells. *Int J Biochem Cell Biol* **37**, 1921-1929 (2005). https://doi.org:10.1016/j.biocel.2005.04.015

35 Gupta, I., Singh, K., Varshney, N. K. & Khan, S. Delineating Crosstalk Mechanisms of the Ubiquitin Proteasome System That Regulate Apoptosis. *Front Cell Dev Biol* **6**, 11 (2018). https://doi.org:10.3389/fcell.2018.00011

36 Ling, Y. H. *et al.* Mechanisms of proteasome inhibitor PS-341-induced G(2)-M-phase arrest and apoptosis in human non-small cell lung cancer cell lines. *Clinical cancer research : an official journal of the American Association for Cancer Research* **9**, 1145-1154 (2003).

37 Nawrocki, S. T. *et al.* Effects of the proteasome inhibitor PS-341 on apoptosis and angiogenesis in orthotopic human pancreatic tumor xenografts. *Mol Cancer Ther* **1**, 1243-1253 (2002).

38 Selimovic, D. *et al.* Bortezomib/proteasome inhibitor triggers both apoptosis and autophagy-dependent pathways in melanoma cells. *Cell Signal* **25**, 308-318 (2013). https://doi.org:10.1016/j.cellsig.2012.10.004

39 Bao, X. *et al.* Bortezomib induces apoptosis and suppresses cell growth and metastasis by inactivation of Stat3 signaling in chondrosarcoma. *Int J Oncol* **50**, 477-486 (2017). https://doi.org:10.3892/ijo.2016.3806

40 Lou, Z. *et al.* Bortezomib induces apoptosis and autophagy in osteosarcoma cells through mitogen-activated protein kinase pathway in vitro. *J Int Med Res* **41**, 1505-1519 (2013). https://doi.org:10.1177/0300060513490618

1009 41 Hofmann, J. F. & Beach, D. cdt1 is an essential target of the Cdc10/Sct1 transcription
1010 factor: requirement for DNA replication and inhibition of mitosis. *EMBO J* **13**, 425-434
1011 (1994). https://doi.org:10.1002/j.1460-2075.1994.tb06277.x
1012 42 Fagundes, R. & Teixeira, L. K. Cyclin E/CDK2: DNA Replication, Replication Stress and
1013 Genomic Instability. *Front Cell Dev Biol* **9**, 774845 (2021).
1014 https://doi.org:10.3389/fcell.2021.774845
1015 43 Caldon, C. E. & Musgrove, E. A. Distinct and redundant functions of cyclin E1 and cyclin
1016 E2 in development and cancer. *Cell Div* **5**, 2 (2010). https://doi.org:10.1186/1747-1028-
1017 5-2
1018 44 Pozo, P. N. & Cook, J. G. Regulation and Function of Cdt1; A Key Factor in Cell
1019 Proliferation and Genome Stability. *Genes (Basel)* **8** (2016).
1020 https://doi.org:10.3390/genes8010002
1021 45 Martinez-Alonso, D. & Malumbres, M. Mammalian cell cycle cyclins. *Semin Cell Dev Biol*
1022 **107**, 28-35 (2020). https://doi.org:10.1016/j.semcdb.2020.03.009
1023 46 Kaufmann, S. H., Desnoyers, S., Ottaviano, Y., Davidson, N. E. & Poirier, G. G. Specific
1024 proteolytic cleavage of poly(ADP-ribose) polymerase: an early marker of chemotherapy-
1025 induced apoptosis. *Cancer Res* **53**, 3976-3985 (1993).
1026 47 Kaufmann, S. H. Induction of endonucleolytic DNA cleavage in human acute
1027 myelogenous leukemia cells by etoposide, camptothecin, and other cytotoxic anticancer
1028 drugs: a cautionary note. *Cancer Res* **49**, 5870-5878 (1989).
1029 48 Boulares, A. H. *et al.* Role of poly(ADP-ribose) polymerase (PARP) cleavage in apoptosis.
1030 Caspase 3-resistant PARP mutant increases rates of apoptosis in transfected cells. *J Biol*
1031 *Chem* **274**, 22932-22940 (1999). https://doi.org:10.1074/jbc.274.33.22932
1032 49 Rager, J. E. in *Systems Biology in Toxicology and Environmental Health* 187-205 (2015).
1033 50 Stewart, E. *et al.* Orthotopic patient-derived xenografts of paediatric solid tumours.
1034 *Nature* **549**, 96-100 (2017). https://doi.org:10.1038/nature23647
1035 51 Murphy, A. J. *et al.* Forty-five patient-derived xenografts capture the clinical and
1036 biological heterogeneity of Wilms tumor. *Nature communications* **10**, 5806 (2019).
1037 https://doi.org:10.1038/s41467-019-13646-9
1038 52 Cerami, E. *et al.* The cBio cancer genomics portal: an open platform for exploring
1039 multidimensional cancer genomics data. *Cancer Discov* **2**, 401-404 (2012).
1040 https://doi.org:10.1158/2159-8290.CD-12-0095
1041 53 Gao, J. J. *et al.* Integrative Analysis of Complex Cancer Genomics and Clinical Profiles
1042 Using the cBioPortal. *Sci Signal* **6** (2013). https://doi.org:ARTN pl1
1043 DOI 10.1126/scisignal.2004088
1044 54 Walz, A. L. *et al.* Recurrent DGCR8, DROSHA, and SIX homeodomain mutations in
1045 favorable histology Wilms tumors. *Cancer cell* **27**, 286-297 (2015).
1046 https://doi.org:10.1016/j.ccell.2015.01.003
1047 55 Wegert, J. *et al.* Mutations in the SIX1/2 pathway and the DROSHA/DGCR8 miRNA
1048 microprocessor complex underlie high-risk blastemal type Wilms tumors. *Cancer cell* **27**,
1049 298-311 (2015). https://doi.org:10.1016/j.ccell.2015.01.002
1050 56 Torrezan, G. T. *et al.* Recurrent somatic mutation in DROSHA induces microRNA profile
1051 changes in Wilms tumour. *Nature communications* **5**, 4039 (2014).
1052 https://doi.org:10.1038/ncomms5039

1053 57 Rakheja, D. *et al.* Somatic mutations in DROSHA and DICER1 impair microRNA biogenesis
1054 through distinct mechanisms in Wilms tumours. *Nature communications* **2**, 4802 (2014).
1055 https://doi.org:10.1038/ncomms5802
1056 58 Tiburcio, P. D. B. *et al.* DROSHA Regulates Mesenchymal Gene Expression in Wilms
1057 Tumor. *Mol Cancer Res* **22**, 711-720 (2024). https://doi.org:10.1158/1541-7786.MCR-23-
1058 0930
1059 59 Matthews, H. K., Bertoli, C. & de Bruin, R. A. M. Cell cycle control in cancer. *Nat Rev Mol*
1060 *Cell Biol* **23**, 74-88 (2022). https://doi.org:10.1038/s41580-021-00404-3
1061 60 Zou, T. & Lin, Z. The Involvement of Ubiquitination Machinery in Cell Cycle Regulation
1062 and Cancer Progression. *Int J Mol Sci* **22** (2021). https://doi.org:10.3390/ijms22115754
1063 61 Alber, A. B. & Suter, D. M. Dynamics of protein synthesis and degradation through the
1064 cell cycle. *Cell Cycle* **18**, 784-794 (2019).
1065 https://doi.org:10.1080/15384101.2019.1598725
1066 62 Mayer, C., Zhao, J., Yuan, X. & Grummt, I. mTOR-dependent activation of the
1067 transcription factor TIF-IA links rRNA synthesis to nutrient availability. *Genes Dev* **18**,
1068 423-434 (2004). https://doi.org:10.1101/gad.285504
1069 63 Mayer, C. & Grummt, I. Ribosome biogenesis and cell growth: mTOR coordinates
1070 transcription by all three classes of nuclear RNA polymerases. *Oncogene* **25**, 6384-6391
1071 (2006). https://doi.org:10.1038/sj.onc.1209883
1072 64 Ni, C. & Buszczak, M. The homeostatic regulation of ribosome biogenesis. *Semin Cell Dev*
1073 *Biol* **136**, 13-26 (2023). https://doi.org:10.1016/j.semcdb.2022.03.043
1074 65 Hua, H. *et al.* Targeting mTOR for cancer therapy. *J Hematol Oncol* **12**, 71 (2019).
1075 https://doi.org:10.1186/s13045-019-0754-1
1076 66 Saxton, R. A. & Sabatini, D. M. mTOR Signaling in Growth, Metabolism, and Disease. *Cell*
1077 **168**, 960-976 (2017). https://doi.org:10.1016/j.cell.2017.02.004
1078 67 Zou, Z., Tao, T., Li, H. & Zhu, X. mTOR signaling pathway and mTOR inhibitors in cancer:
1079 progress and challenges. *Cell Biosci* **10**, 31 (2020). https://doi.org:10.1186/s13578-020-
1080 00396-1
1081 68 Park, S. H., Choi, W. H. & Lee, M. J. Effects of mTORC1 inhibition on proteasome activity
1082 and levels. *BMB Rep* **55**, 161-165 (2022).
1083 https://doi.org:10.5483/BMBRep.2022.55.4.032
1084 69 Williams, R. D. *et al.* Multiple mechanisms of MYCN dysregulation in Wilms tumour.
1085 *Oncotarget* **6**, 7232-7243 (2015). https://doi.org:10.18632/oncotarget.3377
1086 70 Bartel, D. P. MicroRNAs: genomics, biogenesis, mechanism, and function. *Cell* **116**, 281-
1087 297 (2004). https://doi.org:10.1016/s0092-8674(04)00045-5
1088 71 Pichavaram, P. *et al.* Oncogenic Cells of Renal Embryonic Lineage Sensitive to the Small-
1089 Molecule Inhibitor QC6352 Display Depletion of KDM4 Levels and Disruption of
1090 Ribosome Biogenesis. *Mol Cancer Ther* **23**, 478-491 (2024).
1091 https://doi.org:10.1158/1535-7163.MCT-23-0312
1092 72 Tye, B. W. *et al.* Proteotoxicity from aberrant ribosome biogenesis compromises cell
1093 fitness. *Elife* **8** (2019). https://doi.org:10.7554/eLife.43002
1094 73 Zhang, Y. & Manning, B. D. mTORC1 signaling activates NRF1 to increase cellular
1095 proteasome levels. *Cell Cycle* **14**, 2011-2017 (2015).
1096 https://doi.org:10.1080/15384101.2015.1044188

1097 74 Zhang, Y. *et al.* Coordinated regulation of protein synthesis and degradation by mTORC1.
1098 *Nature* **513**, 440-443 (2014). https://doi.org:10.1038/nature13492
1099 75 Zhao, J., Zhai, B., Gygi, S. P. & Goldberg, A. L. mTOR inhibition activates overall protein
1100 degradation by the ubiquitin proteasome system as well as by autophagy. *Proc Natl Acad*
1101 *Sci U S A* **112**, 15790-15797 (2015). https://doi.org:10.1073/pnas.1521919112
1102 76 Kaiser, M. S. *et al.* Dual roles of mTORC1-dependent activation of the ubiquitin-
1103 proteasome system in muscle proteostasis. *Commun Biol* **5**, 1141 (2022).
1104 https://doi.org:10.1038/s42003-022-04097-y
1105 77 Chen, D., Frezza, M., Schmitt, S., Kanwar, J. & Dou, Q. P. Bortezomib as the First
1106 Proteasome Inhibitor Anticancer Drug: Current Status and Future Perspectives. *Current*
1107 *Cancer Drug Targets* **11**, 239-253 (2011). https://doi.org:Doi
1108 10.2174/156800911794519752
1109 78 Leonardo-Sousa, C. *et al.* Revisiting Proteasome Inhibitors: Molecular Underpinnings of
1110 Their Development, Mechanisms of Resistance and Strategies to Overcome Anti-Cancer
1111 Drug Resistance. *Molecules* **27** (2022). https://doi.org:10.3390/molecules27072201
1112 79 Lu, S. & Wang, J. The resistance mechanisms of proteasome inhibitor bortezomib.
1113 *Biomark Res* **1**, 13 (2013). https://doi.org:10.1186/2050-7771-1-13
1114 80 August, K. J., Guest, E. M., Lewing, K., Hays, J. A. & Gamis, A. S. Treatment of children
1115 with relapsed and refractory acute lymphoblastic leukemia with mitoxantrone,
1116 vincristine, pegaspargase, dexamethasone, and bortezomib. *Pediatr Blood Cancer* **67**,
1117 e28062 (2020). https://doi.org:10.1002/pbc.28062
1118 81 Teachey, D. T. *et al.* Children's Oncology Group Trial AALL1231: A Phase III Clinical Trial
1119 Testing Bortezomib in Newly Diagnosed T-Cell Acute Lymphoblastic Leukemia and
1120 Lymphoma. *Journal of clinical oncology : official journal of the American Society of*
1121 *Clinical Oncology* **40**, 2106-2118 (2022). https://doi.org:10.1200/JCO.21.02678
1122 82 Styczynski, J., Olszewska-Slonina, D., Kolodziej, B., Napieraj, M. & Wysocki, M. Activity of
1123 bortezomib in glioblastoma. *Anticancer Res* **26**, 4499-4503 (2006).
1124 83 Huang, Z. *et al.* Efficacy of therapy with bortezomib in solid tumors: a review based on
1125 32 clinical trials. *Future Oncol* **10**, 1795-1807 (2014). https://doi.org:10.2217/fon.14.30
1126 84 Manasanch, E. E. & Orlowski, R. Z. Proteasome inhibitors in cancer therapy. *Nat Rev Clin*
1127 *Oncol* **14**, 417-433 (2017). https://doi.org:10.1038/nrclinonc.2016.206
1128 85 Liu, J., Zhao, R., Jiang, X., Li, Z. & Zhang, B. Progress on the Application of Bortezomib and
1129 Bortezomib-Based Nanoformulations. *Biomolecules* **12** (2021).
1130 https://doi.org:10.3390/biom12010051
1131 86 Weyburne, E. S. *et al.* Inhibition of the Proteasome beta2 Site Sensitizes Triple-Negative
1132 Breast Cancer Cells to beta5 Inhibitors and Suppresses Nrf1 Activation. *Cell Chem Biol* **24**,
1133 218-230 (2017). https://doi.org:10.1016/j.chembiol.2016.12.016
1134 87 Hill, C. R. *et al.* Characterisation of the clinical pharmacokinetics of actinomycin D and
1135 the influence of ABCB1 pharmacogenetic variation on actinomycin D disposition in
1136 children with cancer. *Clin Pharmacokinet* **53**, 741-751 (2014).
1137 https://doi.org:10.1007/s40262-014-0153-2
1138 88 Chang, D., Chen, F., Zhang, F., McKay, B. C. & Ljungman, M. Dose-dependent effects of
1139 DNA-damaging agents on p53-mediated cell cycle arrest. *Cell Growth Differ* **10**, 155-162
1140 (1999).

1141 89 Chen, C. S. *et al.* AKT mediates actinomycin D-induced p53 expression. *Oncotarget* **5**,
1142 693-703 (2014). https://doi.org:10.18632/oncotarget.1328
1143 90 Yang, V. W. in *Physiology of the Gastrointestinal Tract* 197-219 (2018).
1144 91 Santo, L., Siu, K. T. & Raje, N. Targeting Cyclin-Dependent Kinases and Cell Cycle
1145 Progression in Human Cancers. *Semin Oncol* **42**, 788-800 (2015).
1146 https://doi.org:10.1053/j.seminoncol.2015.09.024
1147 92 Chu, C., Geng, Y., Zhou, Y. & Sicinski, P. Cyclin E in normal physiology and disease states.
1148 *Trends Cell Biol* **31**, 732-746 (2021). https://doi.org:10.1016/j.tcb.2021.05.001
1149 93 Voutsadakis, I. A. Proteasome expression and activity in cancer and cancer stem cells.
1150 *Tumour Biol* **39**, 1010428317692248 (2017).
1151 https://doi.org:10.1177/1010428317692248
1152 94 Lagadec, C. *et al.* Tumor cells with low proteasome subunit expression predict overall
1153 survival in head and neck cancer patients. *BMC Cancer* **14**, 152 (2014).
1154 https://doi.org:10.1186/1471-2407-14-152
1155 95 Byers, H. A. *et al.* Evaluation of the NRF1-proteasome axis as a therapeutic target in
1156 breast cancer. *Sci Rep* **13**, 15843 (2023). https://doi.org:10.1038/s41598-023-43121-x
1157 96 He, W. *et al.* PSMB2 plays an oncogenic role in glioma and correlates to the immune
1158 microenvironment. *Sci Rep* **14**, 5861 (2024). https://doi.org:10.1038/s41598-024-56493-
1159 5
1160 97 Liu, J., Mi, J., Liu, S., Chen, H. & Jiang, L. PSMB5 overexpression is correlated with tumor
1161 proliferation and poor prognosis in hepatocellular carcinoma. *FEBS Open Bio* **12**, 2025-
1162 2041 (2022). https://doi.org:10.1002/2211-5463.13479
1163 98 Walerych, D. *et al.* Proteasome machinery is instrumental in a common gain-of-function
1164 program of the p53 missense mutants in cancer. *Nat Cell Biol* **18**, 897-909 (2016).
1165 https://doi.org:10.1038/ncb3380
1166 99 Schindelin, J. *et al.* Fiji: an open-source platform for biological-image analysis. *Nat*
1167 *Methods* **9**, 676-682 (2012). https://doi.org:10.1038/nmeth.2019
1168 100 Ju, Z. *et al.* Development of a robust classifier for quality control of reverse-phase
1169 protein arrays. *Bioinformatics (Oxford, England)* **31**, 912-918 (2015).
1170 https://doi.org:10.1093/bioinformatics/btu736
1171 101 Shehwana, H. *et al.* RPPA SPACE: an R package for normalization and quantitation of
1172 Reverse-Phase Protein Array data. *Bioinformatics (Oxford, England)* **38**, 5131-5133
1173 (2022). https://doi.org:10.1093/bioinformatics/btac665
1174 102 Siwak, D. R., Li, J., Akbani, R., Liang, H. & Lu, Y. Analytical Platforms 3: Processing Samples
1175 via the RPPA Pipeline to Generate Large-Scale Data for Clinical Studies. *Adv Exp Med Biol*
1176 **1188**, 113-147 (2019). https://doi.org:10.1007/978-981-32-9755-5_7
1177 103 Hoff, F. W., Lu, Y. & Kornblau, S. M. Antibody Screening. *Adv Exp Med Biol* **1188**, 149-163
1178 (2019). https://doi.org:10.1007/978-981-32-9755-5_8
1179 104 McGlincy, N. J. & Ingolia, N. T. Transcriptome-wide measurement of translation by
1180 ribosome profiling. *Methods* **126**, 112-129 (2017).
1181 https://doi.org:10.1016/j.ymeth.2017.05.028
1182 105 Ingolia, N. T., Brar, G. A., Rouskin, S., McGeachy, A. M. & Weissman, J. S. The ribosome
1183 profiling strategy for monitoring translation in vivo by deep sequencing of ribosome-

1184 protected mRNA fragments. *Nature protocols* **7**, 1534 (2012).
1185 https://doi.org:10.1038/nprot.2012.086
1186 https://www.nature.com/articles/nprot.2012.086#supplementary-information
1187 106 Han, Y. *et al.* Monitoring cotranslational protein folding in mammalian cells at codon
1188 resolution. *Proc Natl Acad Sci U S A* **109**, 12467-12472 (2012).
1189 https://doi.org:10.1073/pnas.1208138109
1190 107 Kim, D., Paggi, J. M., Park, C., Bennett, C. & Salzberg, S. L. Graph-based genome
1191 alignment and genotyping with HISAT2 and HISAT-genotype. *Nat Biotechnol* **37**, 907-915
1192 (2019). https://doi.org:10.1038/s41587-019-0201-4
1193 108 Pertea, M. *et al.* StringTie enables improved reconstruction of a transcriptome from
1194 RNA-seq reads. *Nat Biotechnol* **33**, 290-295 (2015). https://doi.org:10.1038/nbt.3122
1195 109 Liberzon, A. *et al.* The Molecular Signatures Database (MSigDB) hallmark gene set
1196 collection. *Cell Syst* **1**, 417-425 (2015). https://doi.org:10.1016/j.cels.2015.12.004
1197 110 Mootha, V. K. *et al.* PGC-1alpha-responsive genes involved in oxidative phosphorylation
1198 are coordinately downregulated in human diabetes. *Nature genetics* **34**, 267-273 (2003).
1199 https://doi.org:10.1038/ng1180
1200 111 Korotkevich, G. *et al.* Fast gene set enrichment analysis. *bioRxiv*, 060012 (2021).
1201 https://doi.org:10.1101/060012
1202 112 Doench, J. G. *et al.* Optimized sgRNA design to maximize activity and minimize off-target
1203 effects of CRISPR-Cas9. *Nat Biotechnol* **34**, 184-191 (2016).
1204 https://doi.org:10.1038/nbt.3437
1205 113 Wang, B. *et al.* Integrative analysis of pooled CRISPR genetic screens using MAGeCKFlute.
1206 *Nature protocols* **14**, 756-780 (2019). https://doi.org:10.1038/s41596-018-0113-7
1207 114 Li, W. *et al.* MAGeCK enables robust identification of essential genes from genome-scale
1208 CRISPR/Cas9 knockout screens. *Genome Biol* **15**, 554 (2014).
1209 https://doi.org:10.1186/s13059-014-0554-4
1210 115 Perry, R. P. & Kelley, D. E. Inhibition of RNA synthesis by actinomycin D: characteristic
1211 dose-response of different RNA species. *J Cell Physiol* **76**, 127-139 (1970).
1212 https://doi.org:10.1002/jcp.1040760202
1213 116 Zheng, S. *et al.* SynergyFinder Plus: Toward Better Interpretation and Annotation of Drug
1214 Combination Screening Datasets. *Genomics Proteomics Bioinformatics* **20**, 587-596
1215 (2022). https://doi.org:10.1016/j.gpb.2022.01.004
1216 117 Love, M. I., Huber, W. & Anders, S. Moderated estimation of fold change and dispersion
1217 for RNA-seq data with DESeq2. *Genome Biol* **15**, 550 (2014).
1218 https://doi.org:10.1186/s13059-014-0550-8
1219

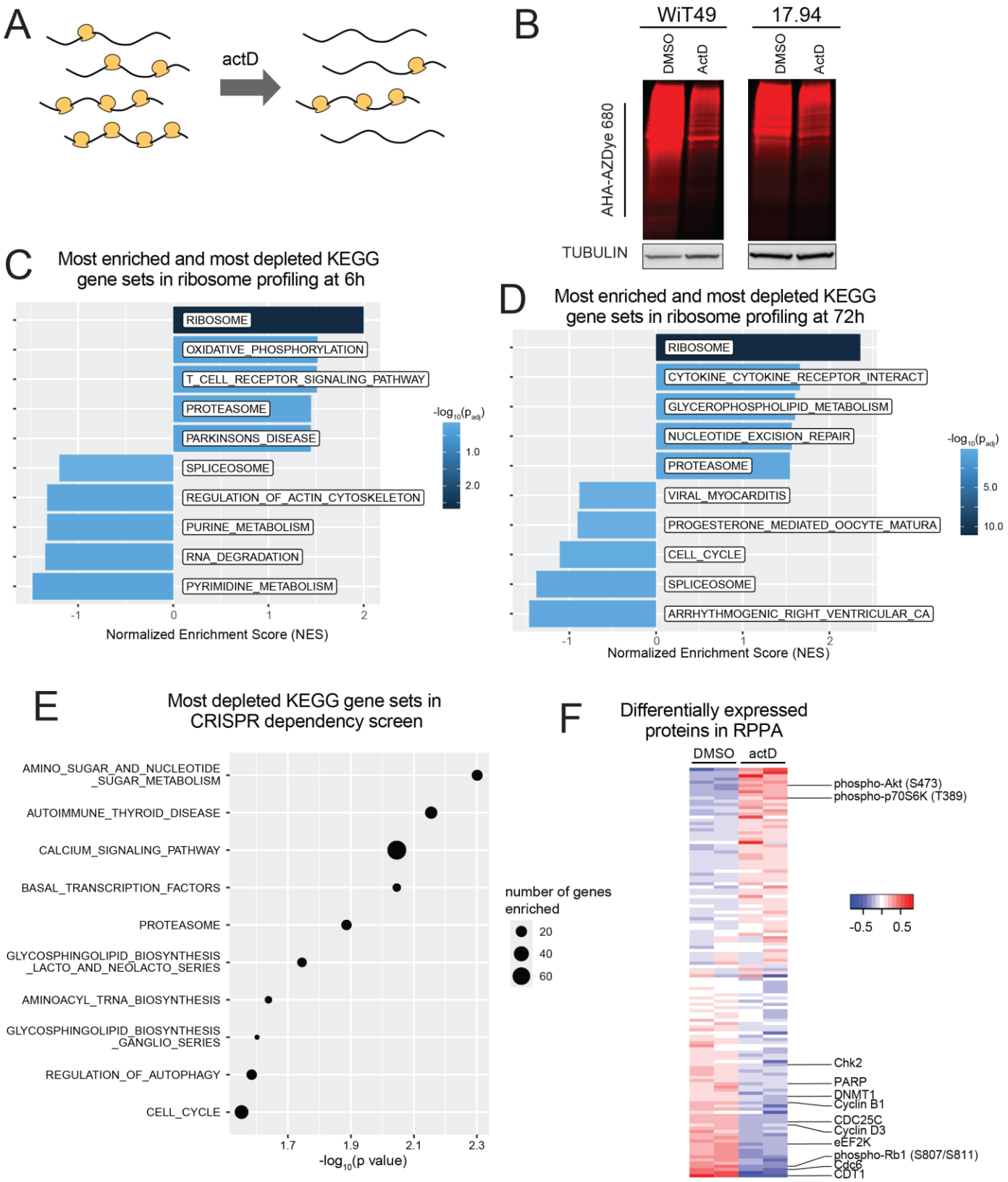

Figure 1. ActD disrupts protein homeostasis in anaplastic Wilms tumor cells
(A) Diagram of the effect of actD at the translational level. ActD depletes fully-formed ribosomes and reduces translational capacity. The reduced ribosomes are distributed unevenly. Ribosome profiling provides a snapshot of transcripts actively undergoing translation. **(B)** Whole protein lysates of DMSO (Vehicle) or actD-treated WiT49 or 17.94 fluorescently labeled with AHA-AZDye 680 for nascent protein detection and corresponding loading control TUBULIN detected by western blot from the same gel. **(C,D)** Top 5 most enriched and bottom 5 most depleted KEGG gene sets in ribosome profiling of actD- vs. DMSO-treated WiT49 after 6 hours **(C)** or 72 hours **(D)**. **(E)** GSEA of genome-wide CRISPR knockout screen reveals top 10 most significant KEGG pathways that sensitize WiT49 to actD, ranked by p-value. **(F)** Heatmap displaying RPPA results of actD- vs. DMSO-treated WiT49. Normalized, log2-transformed, median-centered values from validated antibodies with standard deviation over 0.1 are shown here.

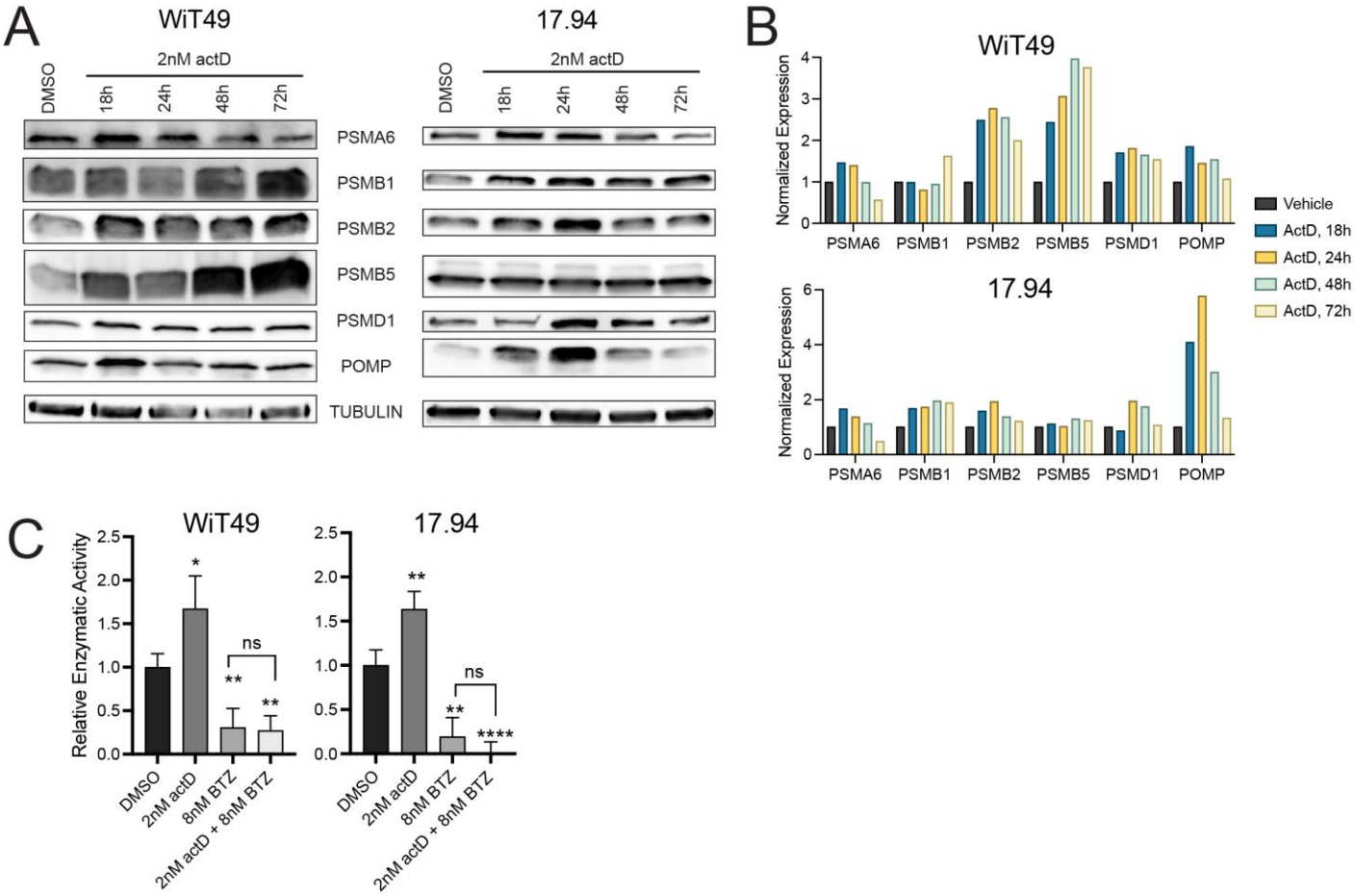

Figure 2. ActD promotes proteasome level and activity in anaplastic Wilms tumor cells
(A,B) Western blots for **(A)** and quantification of **(B)** proteasome subunits PSMA6 (α1), PSMB1 (β6), PSMB2 (β4), PSMB5 (β5), and PSMD1 (P112), and POMP in WiT49 and 17.94 following 18-, 24-, 48-, and 72-hour 2nM actD treatment versus vehicle (DMSO). **(C)** Quantification of relative proteasome-specific chymotrypsin-like activity in WiT49 and 17.94 cells following 24 hours of DMSO versus 2nM actD, 8nM BTZ, or 2nM actD + 8nM BTZ treatments (Student's t-test p-value versus vehicle: *<0.05, ** <0.01, ****<0.0001).

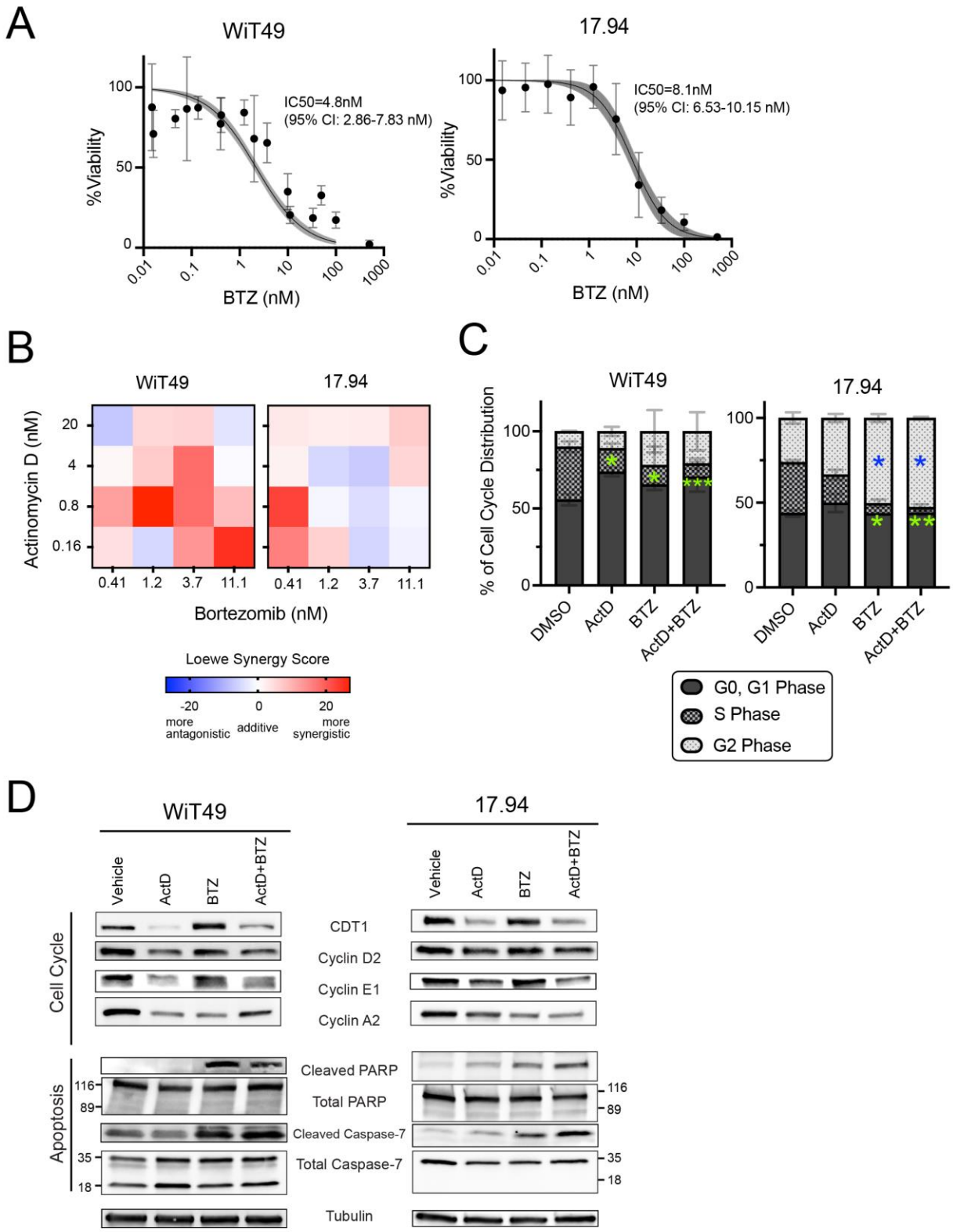

Figure 3. BTZ sensitizes anaplastic Wilms tumor cell lines to actD in vitro

(A) BTZ kill curves for WiT49 and 17.94 with IC50 values indicated (four-point regression line with shaded region representing 95% confidence interval). **(B)** Heat maps of Loewe synergy scores for combinations of actD and BTZ in WiT49 and 17.94 cells. **(C)** Distribution across phases of the cell cycle in WiT49 and 17.94 cells treated with DMSO, actD, BTZ, or combination actD + BTZ for 48 hours. (Student's t-test for treated cells versus DMSO: * <0.05, **<0.01, ***0.001; G0,G1 Phase shown in green, and S Phase in blue). **(D)** Effect of 48-hour treatment WiT49 and 17.94 cells with DMSO, actD, BTZ, and combination actD + BTZ on levels of cell cycle and apoptosis markers by Western blot.

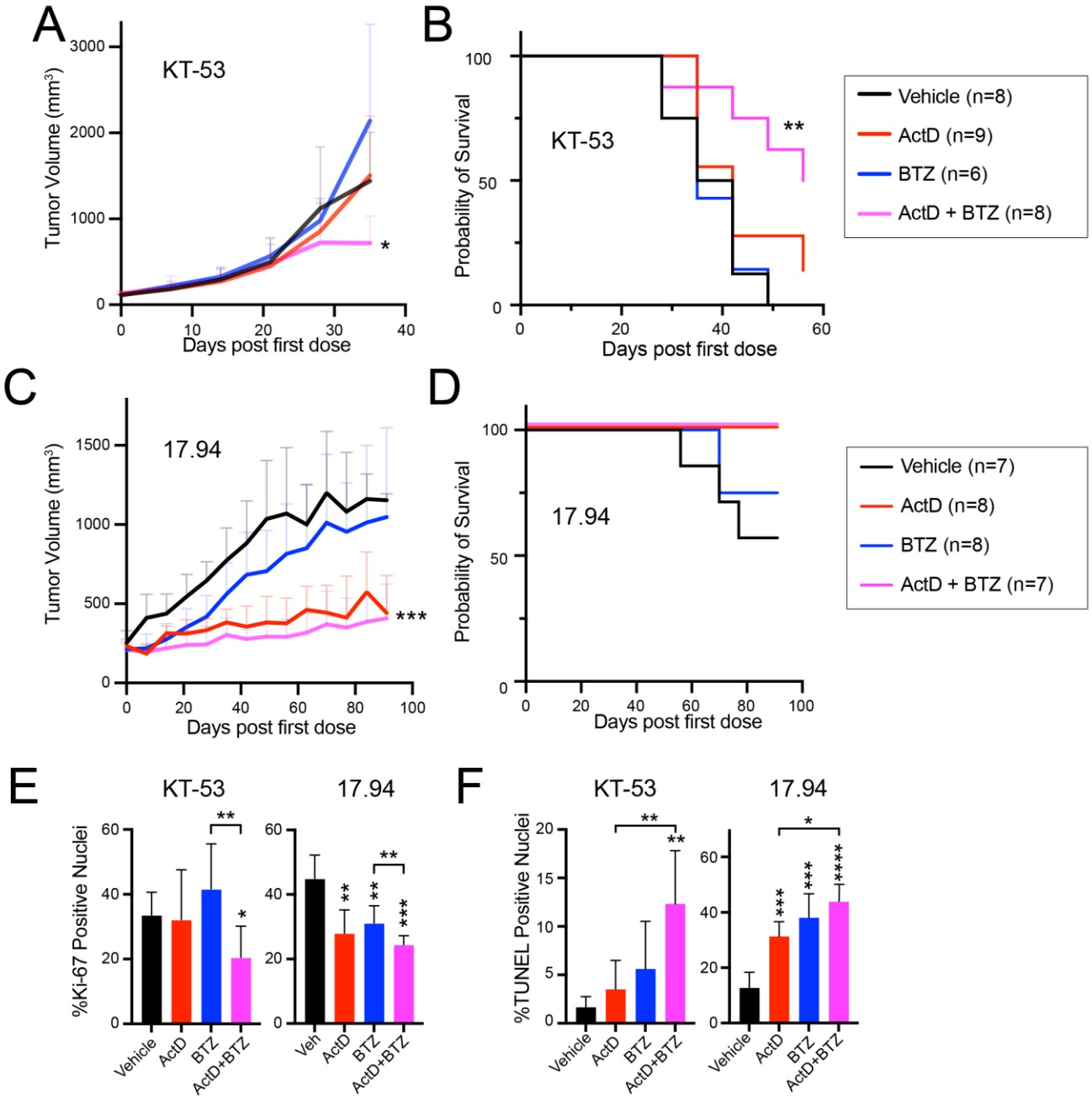

Figure 4. BTZ sensitizes subcutaneous anaplastic Wilms tumor xenografts to actD

(A) Subcutaneous tumor volumes of NSG mice bearing KT-53 xenografts treated with vehicle, actD, BTZ, and combination actD + BTZ (Student's t-test of endpoint volumes of combination versus vehicle or actD only: * <0.05). **(B)** Kaplan-Meier survival curves for KT-53 tumor-bearing mice treated with vehicle, actD only, BTZ only, and combination (log-rank test versus vehicle ** <0.01).**(C)** Subcutaneous tumor volumes of NSG mice bearing 17.94 xenografts treated with vehicle, actD only, BTZ only, and combination (Student's t-test of endpoint volumes of combination versus vehicle: ***<0.001). **(D)** Kaplan-Meier survival curves for 17.94 tumor-bearing mice treated with vehicle, actD only, BTZ only, and combination. **(E,F)** Quantification of Ki-67 positive nuclei (E) and TUNEL positive nuclei (F) in in KT-53 and 17.94 subcutaneous tumors treated with vehicle, actD only, BTZ only, or combination actD + BTZ (Student's t-test p-value versus vehicle unless otherwise indicated: * <0.05, **<0.01, ***<0.001, ****<0.0001).

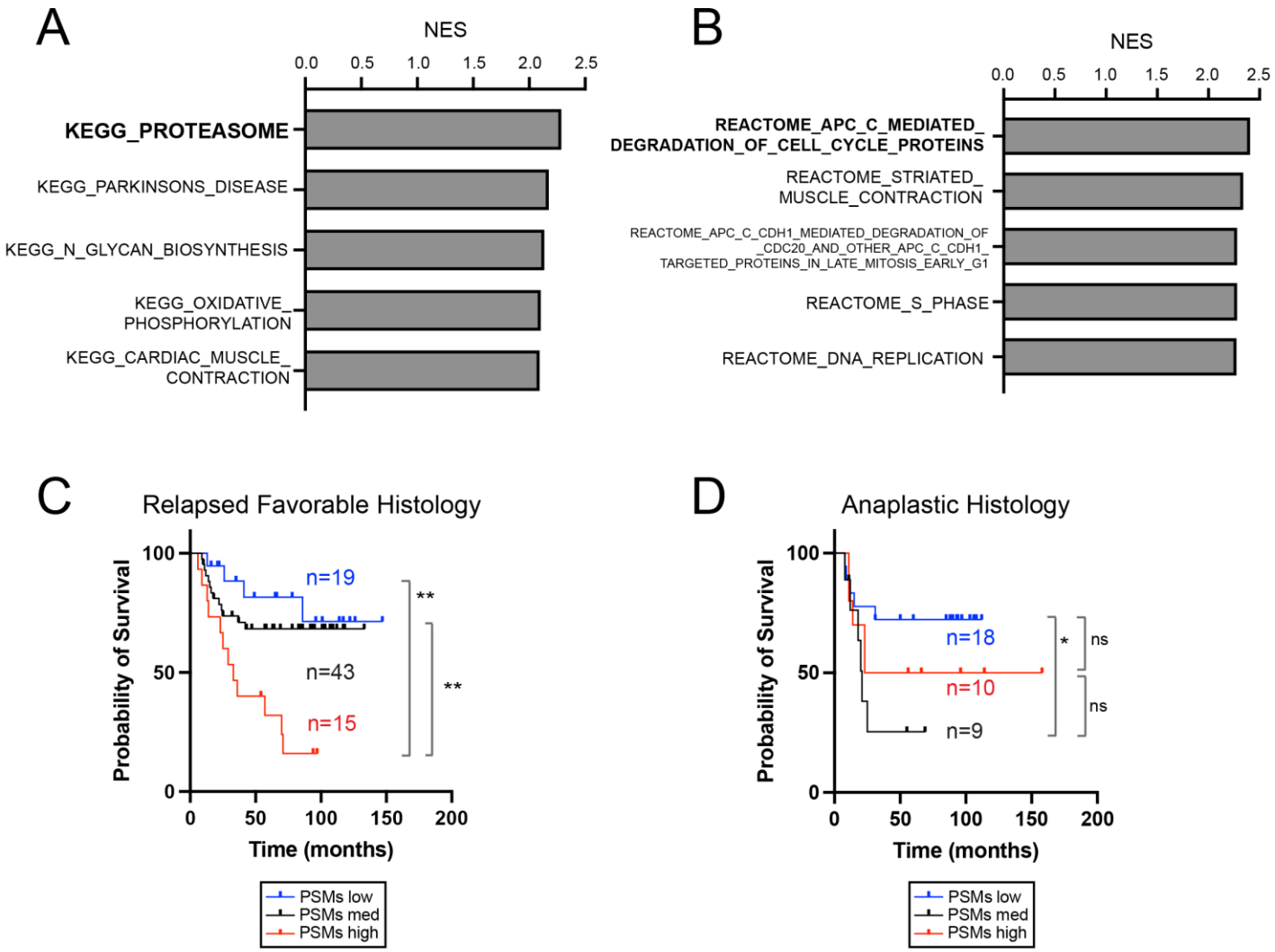

Figure 5. RNA expression of proteasome genes in TARGET anaplastic histology and relapsed favorable histology Wilms tumors

(A) Top KEGG pathways enriched in RNA-seq of DAWT versus rFHWT. **(B)** Top reactome pathways enriched in RNA-seq of DAWT versus rFHWT. **(C,D)** Overall survival of Wilms tumor patients stratified according to expression of proteasome enzymatic subunit genes PSMB1, PSMB2, PSMB5 among patients with relapsed favorable histology tumors **(C)** or anaplastic histology tumors **(D)**. (Log Rank test p-value: *<0.05, ** 0.01)

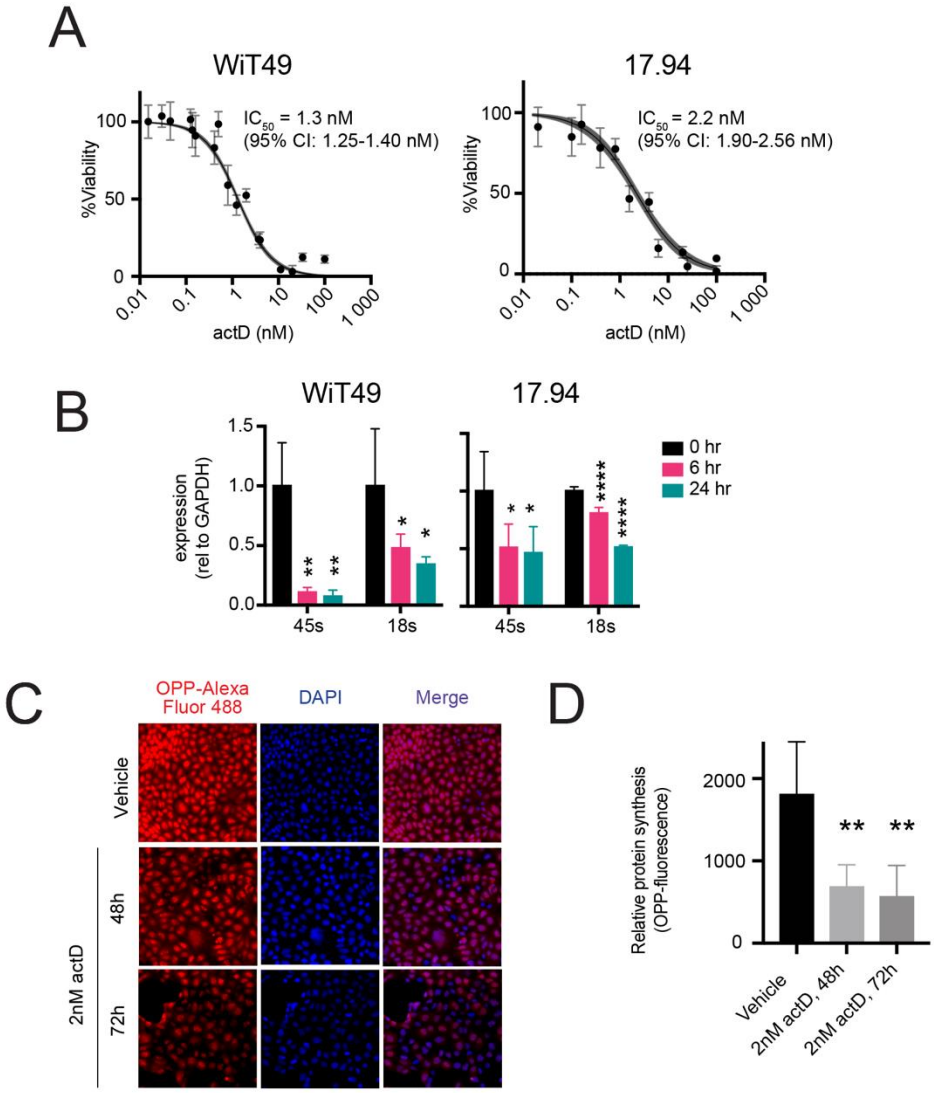

Supplementary Figure S1. ActD alters global translation in WiT49 anaplastic Wilms tumor cells
(A) ActD kill curves for anaplastic Wilms Tumor cell lines WiT49 and 17.94 with IC50 values indicated (four-point regression line with shaded region representing 95% confidence interval). **(B)** Levels of 45s pre-rRNA and 18s mature rRNA in anaplastic Wilms tumor cell lines WiT49 and 17.94, quantified by qPCR following actD treatment for 6 and 24 hours. **(C,D)** Micrographs **(C)** and quantification **(D)** of protein synthesis assay. Red fluorescence measures O-propargyl-puromycin (OPP) incorporation relative to total area of WiT49 cells treated with 48 and 72 hours of 2nM actD or vehicle DMSO. (Student's t-test vs. vehicle, ** $p<0.01$.)

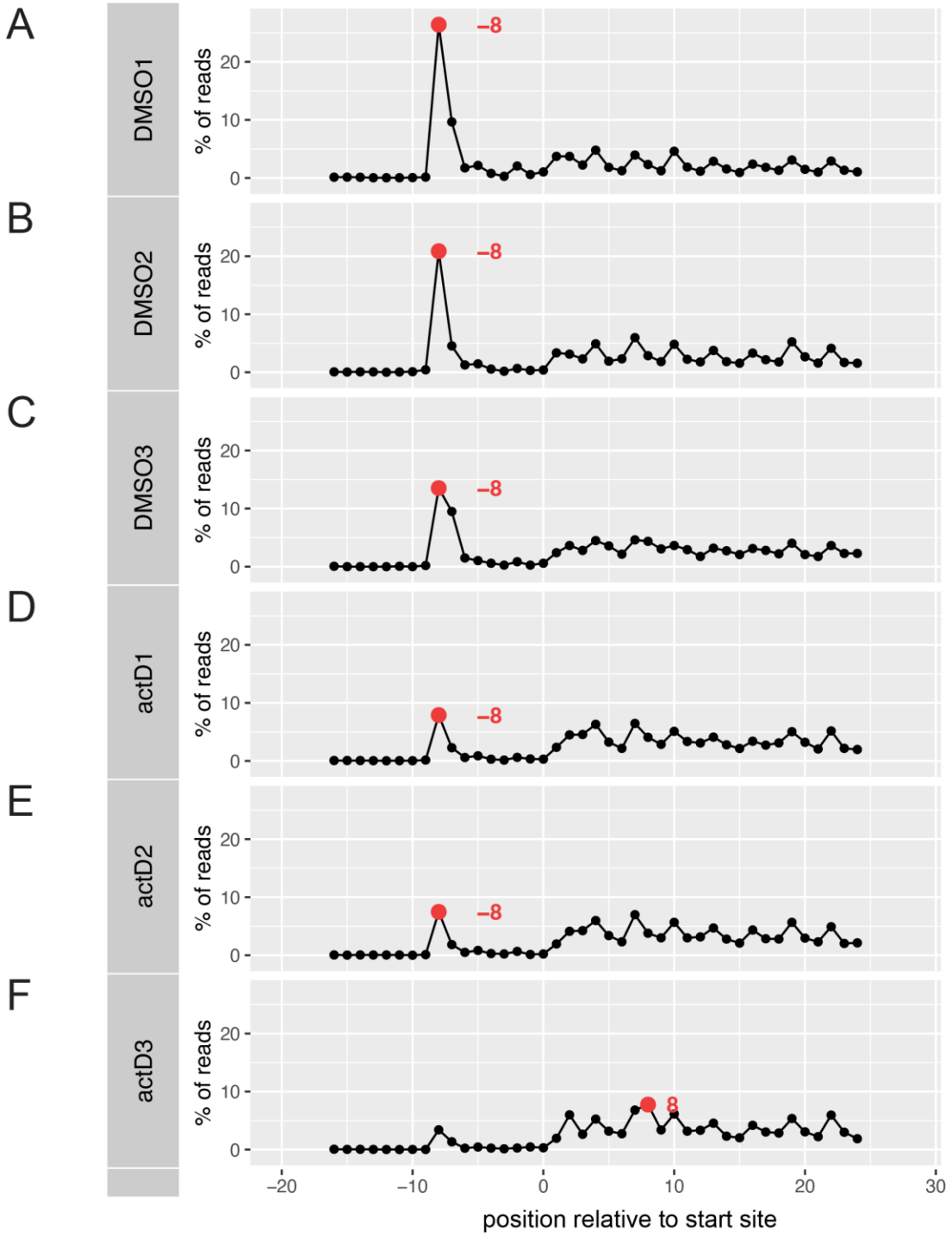

Supplementary Figure S2. Ribosome footprints are depleted at translation initiation sites in actD-treated WiT49.

(A-F) Proportion of left edge of ribosome footprints (y-axis) relative to translation initiation site (0 on x-axis), on the top 30% most abundant transcripts, in samples treated with DMSO **(A-C)** or actD **(D-F)** at 72 hours. Peak position highlighted in red.

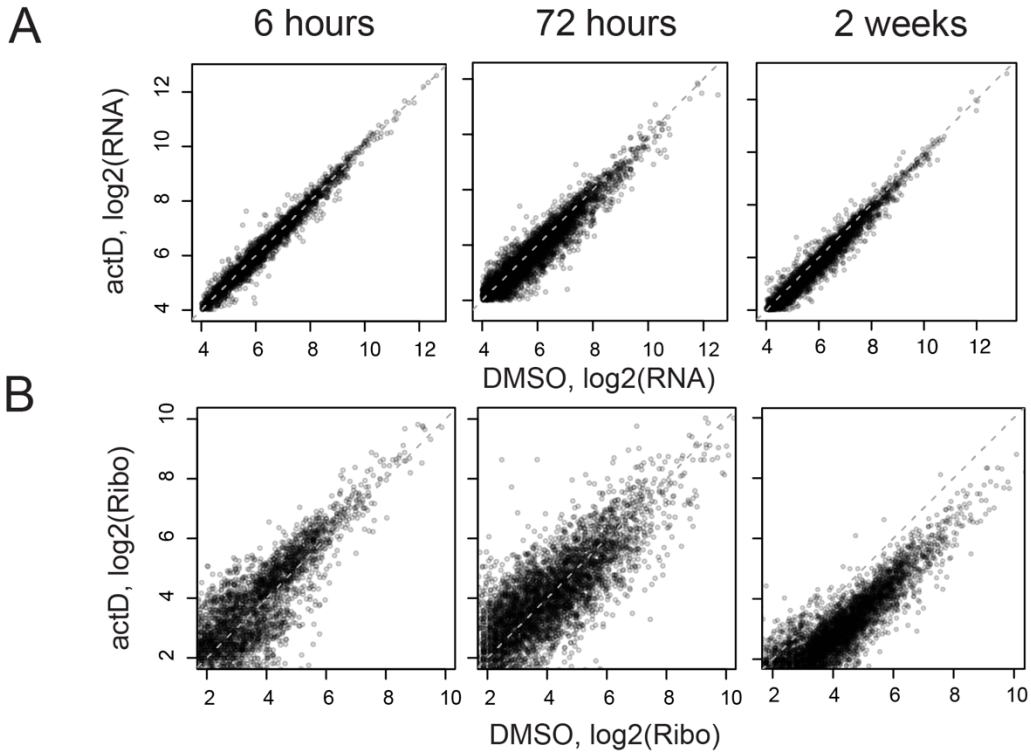

Supplementary Figure S3. Ribosome profiling metrics in actD-treated WiT49.
(A,B) Log2-transformed counts aligning to each gene, by RNA-seq **(A)** and translation efficiency by ribosome profiling **(B)** after 6-hour, 72-hour, and 2-week treatments of WiT49 with actD (y-axes) versus DMSO (x-axes).

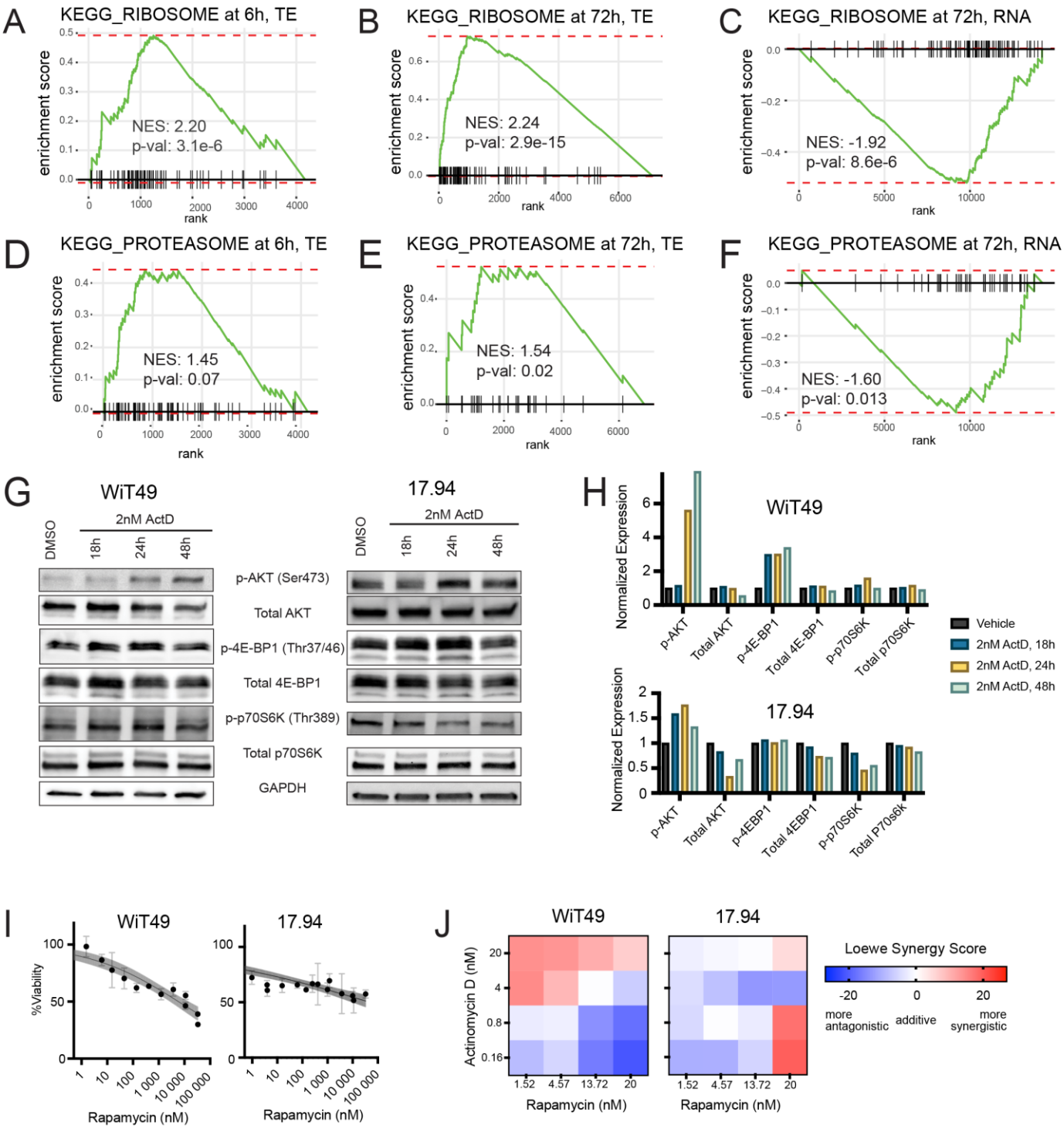

Supplementary Figure S4. ActD induces translation of ribosome and proteasome subunits and upregulates Akt/mTOR signaling.

(A,B) KEGG_RIBOSOME gene set enrichment plots for translational efficiency (TE) after 6 hours **(A)** and 72 hours **(B)** of actD vs. DMSO. NES, normalized enrichment score. **(C)** KEGG_RIBOSOME gene set enrichment plot for RNA expression after 72 hours of actD vs. DMSO. **(D,E)** KEGG_PROTEASOME gene set enrichment plots for TE after 6 hours **(D)** and 72 hours **(E)** of actD vs. DMSO. **(F)** KEGG_PROTEASOME gene set enrichment plot for RNA expression after 72 hours of actD vs. DMSO. **(G,H)** Phosphorylation of Akt/mTOR signaling components visualized and quantified by Western blot in WiT49 and 17.94 following 2nM actD. **(I)** Rapamycin kill curves for anaplastic Wilms tumor cell lines WiT49 and 17.94 (four-point regression line with shaded region representing 95% confidence interval). **(J)** Heat maps of Loewe synergy scores for combinations of actD and rapamycin in WiT49 and 17.94 cells.

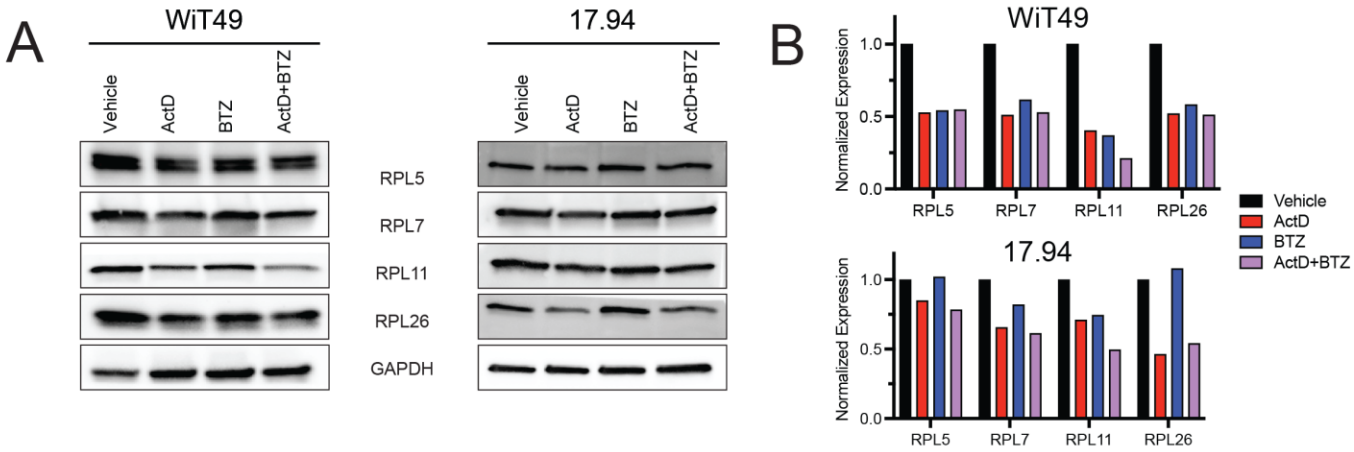

Supplementary Figure S5. ActD and BTZ affect ribosomal protein levels.
(A) Western blots for and quantification **(B)** of ribosomal protein subunits RPL5, RPL7, RPL11, and RPL26 in WiT49 and 17.94 following 48-hour treatment of DMSO, 2nM actD, 8nM BTZ, or 2nM actD + 8nM BTZ.

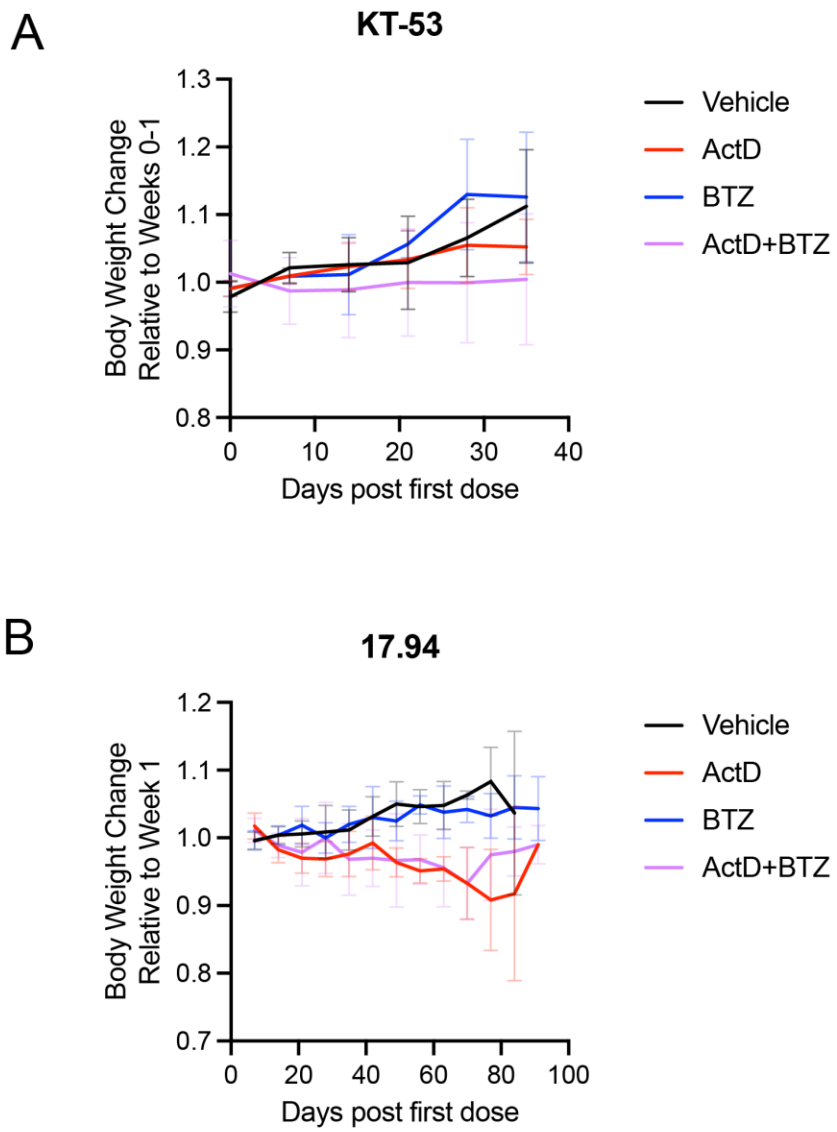

Supplementary Figure S6. Body weight changes in mice treated with actD, BTZ, or combination. **(A,B)** Relative body weight of mice bearing KT-53 xenografts **(A)** or 17.94 xenografts **(B)**, during treatment with actD, BTZ, or both.

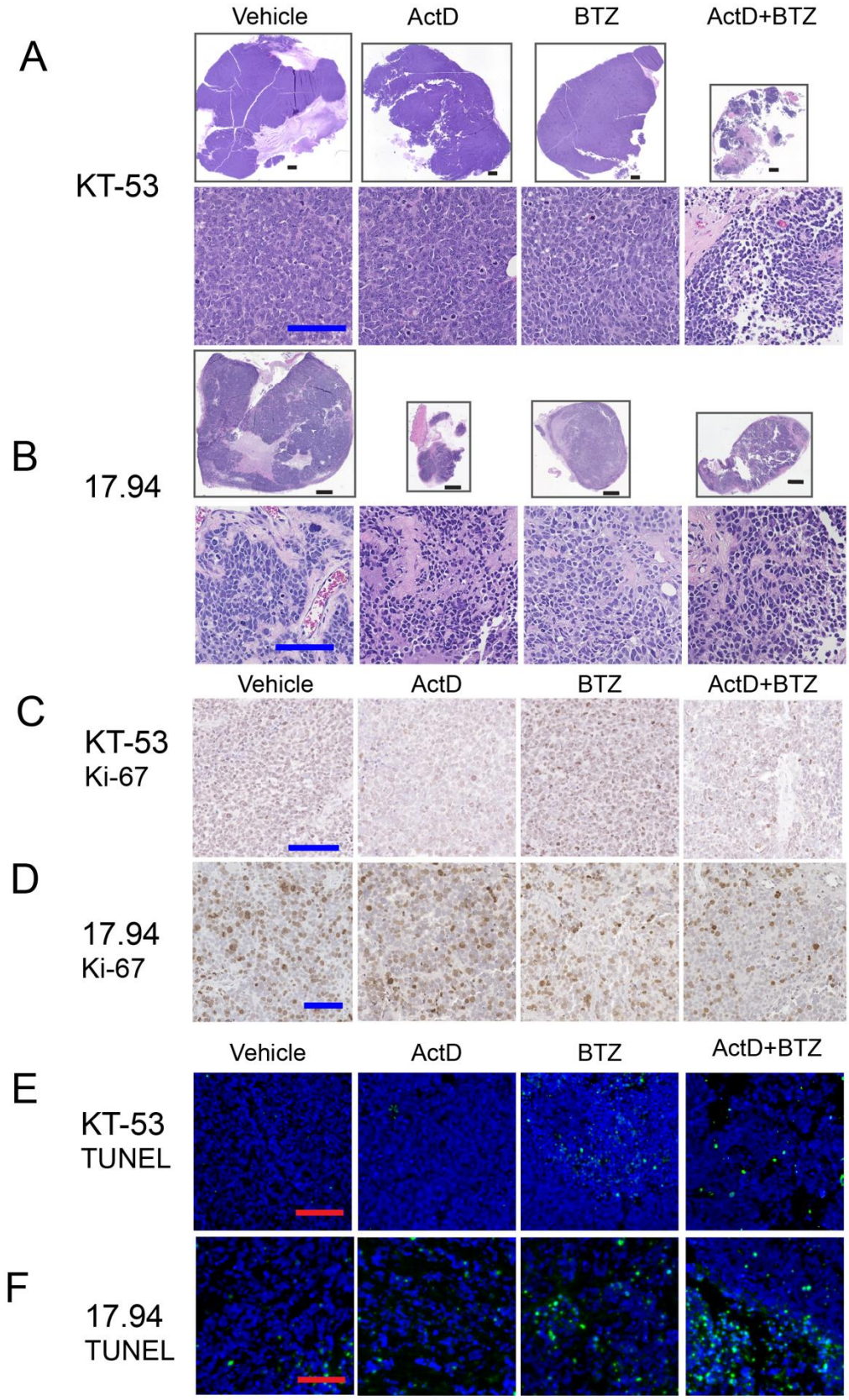

Supplementary Figure S7. Bortezomib enhances cytotoxicity of actinomycin D in anaplastic Wilms tumor xenografts.

(A,B) Low-power and high-power H&E images of **(A)** KT-53 and **(B)** 17.94 subcutaneous tumors (Black bar = 1.0 mm; Blue Bar =100 μm) **(C, D)** High-power photomicrographs of Ki-67 immunohistochemistry of KT-53 (Bar =100 μm) **(C)** and 17.94 **(D)**. **(E, F)** High-power photomicrographs of TUNEL stain of KT-53 (Bar =100 μm) **(E)** and 17.94 **(F)**.

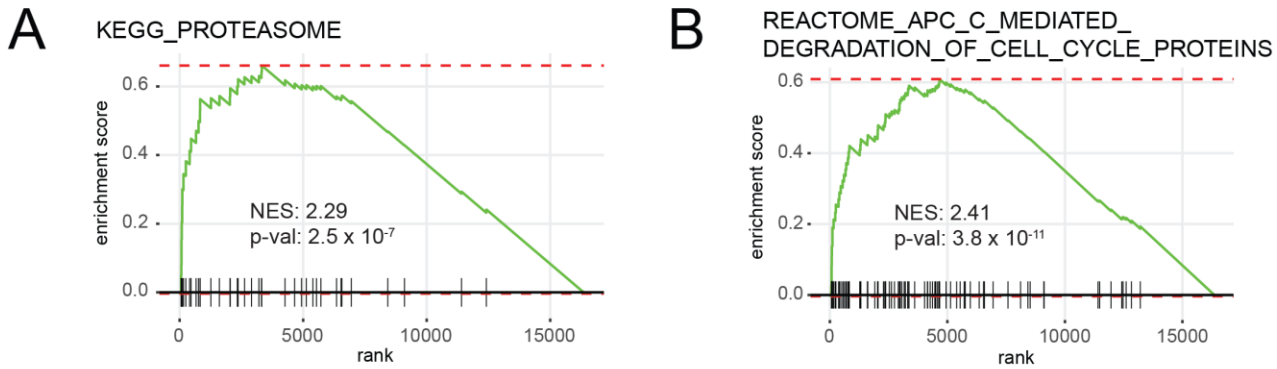

Supplementary Figure S8. Enrichment for proteasome gene sets in anaplastic Wilms tumor. **(A,B)** GSEA plot showing enrichment for KEGG_PROTEASOME **(A)** and REACTOME_APC_C_MEDIATED_DEGRADATION_OF_CELL_CYCLE_PROTEINS **(B)** in anaplastic Wilms tumor vs. relapsed favorable-histology Wilms tumors in TARGET dataset.

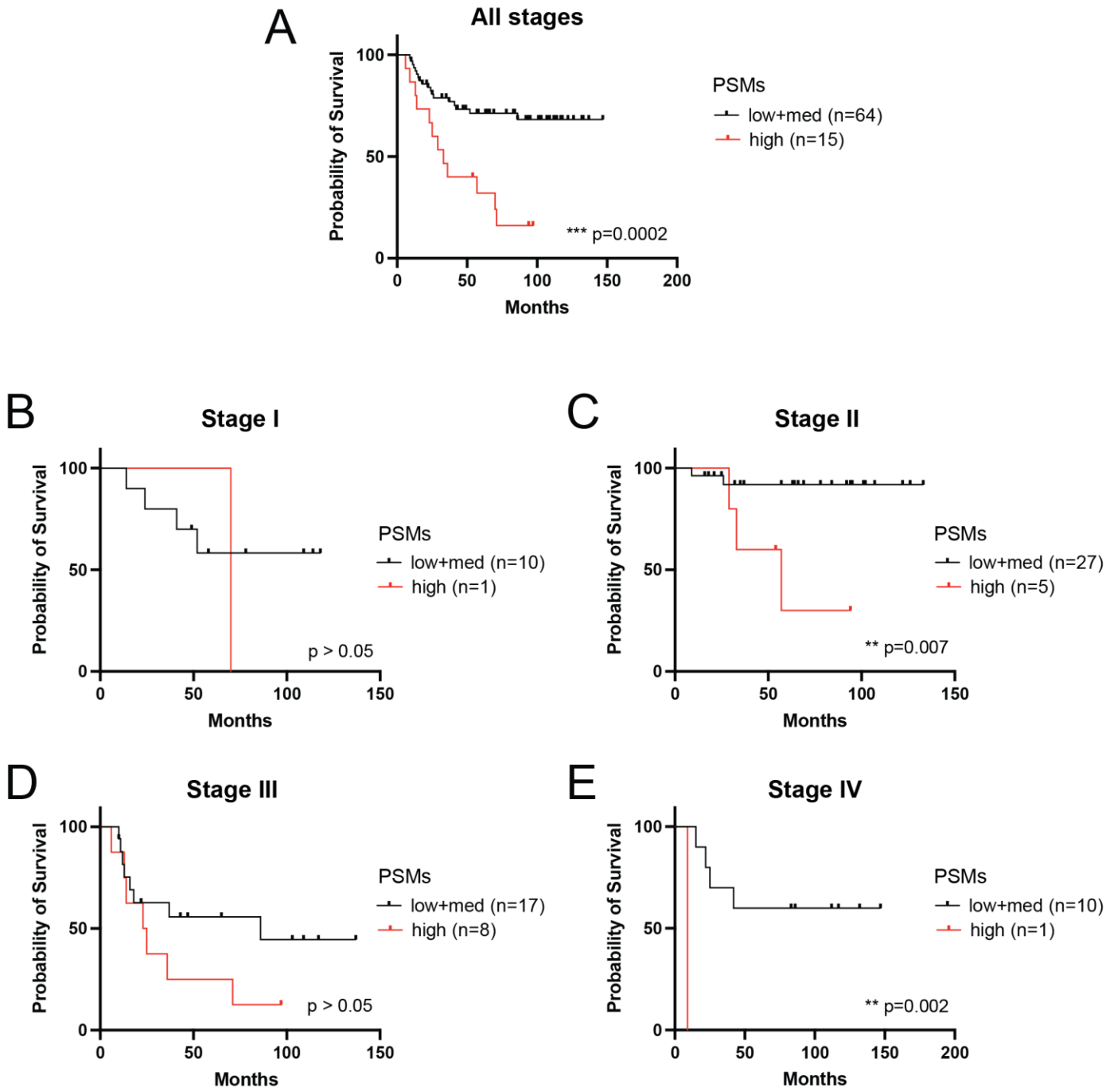

Supplementary Figure S9. Survival of relapsed favorable histology Wilms tumor (FHWT) by stage and proteasome expression.

(A) Overall survival of all relapsed FHWT in TARGET, stratified according to expression of proteasome enzymatic subunit genes *PSMB1*, *PSMB2*, *PSMB5*. **(B-E)** Overall survival of relapsed FHWT in TARGET, for Stages I, II, III, and IV at diagnosis, stratified according to expression of proteasome enzymatic subunit genes *PSMB1*, *PSMB2*, *PSMB5*. (Log rank test p-value: *<0.05, ** < 0.01, *** 0.001).

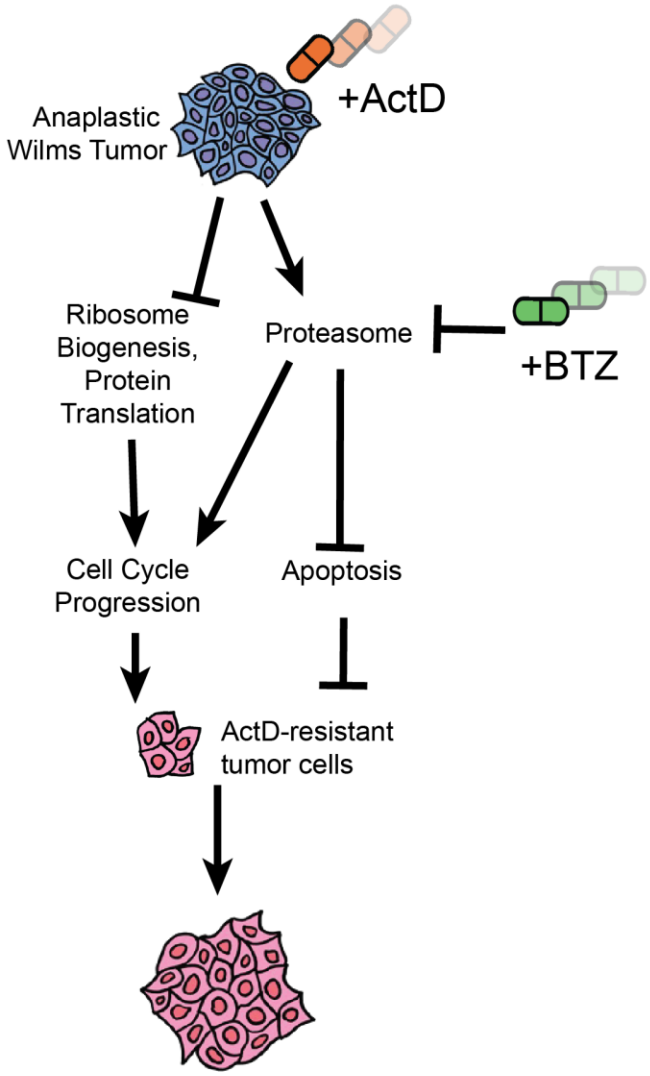

Supplementary Figure S10. Model for effect of actinomycin D on protein homeostasis in Wilms tumor cells.